Finescale Parameterizations of Turbulent Dissipation*

KURT L. POLZIN

School of Oceanography, University of Washington, Seattle, Washington

JOHN M. TOOLE AND RAYMOND W. SCHMITT

Department of Physical Oceanography, Woods Hole Oceanographic Institution, Woods Hole, Massachusetts

(Manuscript received 27 May 1993, in final form 2 May 1994)

ABSTRACT

Fine- and microstructure data from a free fall profiler are analyzed to test models that relate the turbulent dissipation rate (ϵ) to characteristics of the internal wave field. The data were obtained from several distinct internal wave environments, yielding considerably more range in stratification and wave properties than has been previously available. Observations from the ocean interior with negligible large-scale flow were examined to address the buoyancy scaling of ϵ. These data exhibited a factor of 140 range in squared buoyancy frequency (N^2) with depth and uniform internal wave characteristics, consistent with the Garrett–Munk spectrum. The magnitude of ϵ and its variation with $N(\epsilon \sim N^2)$ was best described by the dynamical model of Henyey et al. A second dynamical model, by McComas and Muller, predicted an appropriate buoyancy scaling but overestimated the observed dissipation rates. Two kinematical dissipation parameterizations predicted buoyancy scalings of $N^{3/2}$; these are shown to be inconsistent with the observations.

Data from wave fields that depart from the canonical GM description are also examined and interpreted with reference to the dynamical models. The measurements came from a warm core ring dominated by strong near-inertial shears, a region of steep topography exhibiting high-frequency internal wave characteristics, and a midocean regime dominated at large wavelengths by an internal tide. Of the dissipation predictions examined, those of the Henyey et al. model in which ϵN^{-2} scales as E^2, where E is the nondimensional spectral shear level, were most consistent with observations. Nevertheless, the predictions for these cases exhibited departures from the observations by more than an order of magnitude. For the present data, these discrepancies appeared most sensitive to the distribution of internal wave frequency, inferred here from the ratio of shear spectral level to that for strain. Application of a frequency-based correction to the Henyey et al. model returned dissipation values consistent with observed estimates to within a factor of 2.

These results indicate that the kinetic energy dissipation rate (and attendant turbulent mixing) is small for the background Garrett and Munk internal wave conditions ($0.25\epsilon N^{-2} \sim 0.7 \times 10^{-5}$ m^2 s^{-1}). Dissipation and mixing become large when wave shear spectral levels are elevated, particularly by high-frequency waves. Thus, internal wave reflection/generation at steep topographic features appear promising candidates for achieving enhanced dissipation and strong diapycnal mixing in the deep ocean that appears required by box models and advection–diffusion balances.

1. Introduction

Turbulence in the ocean interior is generally presumed to be driven by vertical shear. In as much as the vast majority of the vertical shear resides in the internal wave field, parameterization of turbulent mixing in the stratified interior of the ocean must address either the dynamical association with internal wave–wave interactions or a kinematical prescription for the mixing associated with a given internal wave environment. In this study the functional dependence (scaling) of the kinetic energy dissipation rate ϵ upon the buoyancy frequency (N) and other parameters related to the internal wave field is defined and compared to existing models by McComas and Muller (1981b), Munk (1981), Gargett and Holloway (1984), and Henyey et al. (1986). This process is facilitated by the fact that the oceanic internal wave field is often well described by the Garrett and Munk (GM) wavenumber/frequency spectrum. [We employ the so-called GM76 spectrum (Garret and Munk 1975, as modified by Cairns and Williams 1976).] Our study begins with an examination of data from the ocean interior in which the wave field is consistent with the GM prescription at depths from 100 to 3000 m (and to which application of the models is most straightforward). The analysis is significant for spanning a wider range in N than previously available [a factor of 2 wider than examined

* Woods Hole Oceanographic Institution Contribution Number 8465.

Corresponding author address: Dr. Kurt L. Polzin, Oceanography WB-10, University of Washington, Seattle, WA 98195.

by Gregg (1989), for example], obtained most notably by inclusion of samples with low stratification below 1000 m. This work thus addresses the buoyancy scaling of ϵ within the GM wave field.

Also of importance are the relationships between internal waves and ϵ in wave fields that depart from the canonical GM prescription. We contribute to this study by examining data from a warm-core ring dominated by strong near-inertial shears, a region adjacent to steep topography exhibiting high-frequency internal wave characteristics and a midocean regime dominated at large wavelengths by an internal tide. The "non-GM" conditions exhibited by these data include varying shear spectral levels (E) and deviations in higher-order spectral characteristics: for example, spectral shapes in vertical wavenumber–frequency space, vertical anisotropy, and horizontal inhomogeneity. (These attributes are multiply combined in the present datasets, potentially complicating the analysis.) In turn, the observations are compared to theoretical predictions based on extensions to the above models that include dependence on the shear spectral level and the shape of the vertical wavenumber and frequency spectra. Theoretical ideas concerning the consequences of anisotropy and inhomogeneity are also noted.

The present work is thematically similar to previous studies, which have sought to empirically test existing model parameterizations of the dissipation rate. There are, however, three important differences: 1) a dataset with expanded range in N as noted above, 2) use of an internally consistent methodology for estimating the spectral level E, and 3) explicit treatment of non-GM spectral characteristics in the model/data comparison. The paper is organized as follows. The (E, N) scalings of the GM-based models are reviewed briefly in section 2a, while section 2b examines some implications of non-GM spectral characteristics for the dynamical models of McComas and Muller (1981b) and Henyey et al. (1986). Details related to data analysis are discussed in section 3. In section 4a the issue of buoyancy scaling is examined through a model–data comparison. Determination of the N scaling in section 4a permits the consequent examination of dissipation scaling in non-GM environments, section 4b. The results are reviewed and discussed in section 5. A summary of the notation appears in Table 1. Details related to the implementation of the model–data comparison are discussed in the two appendixes.

The current work examines, in part, the issue of how ϵ varies with the level and shape of the vertical wavenumber spectrum. It is opportune to recall the structure of the canonical vertical wavenumber shear spectrum discussed by Gargett et al. (1981). The observed spectral density [$S_z(m)$] has a tendency to be constant (i.e., the shear spectrum is white, consistent with GM) up to a cutoff wavenumber m_c and thereafter falls as m^{-1}. Of course, the canonical spectrum set forth by Gargett et al. (1981) is not universal. Both Duda and Cox (1989) and Gregg et al. (1993a) point to quantitative variations. However, the theoretical models discussed in section 2 explicitly appeal to this form in their development. Thus, the canonical spectrum is a necessary as well as useful construct.

The theories we examine derive expressions for the dissipation rate in terms of various measures of the internal wavefield intensity: energy density, shear spectral density, total energy, and/or shear variance. While one can freely convert between energy density and shear spectral density by using the relationship

$$m^2 \frac{d\hat{E}}{dm} = S_z + N^2 F_z,$$

the conversion between total energy, spectral level, and shear variance requires the observed spectra to be well represented by the GM model. In endeavoring to develop a metric of the wave field in our observations consistent with these theoretical treatments, we selected E, the average shear spectral density for wavenumbers less than m_c (see section 3b). Our use of the shear spectral level as a measure of wave state is dictated by the fact that, in general, the measurements reported here do not fully resolve the low wavenumber (energy containing) portion of the vertical wavenumber spectrum. However, we find comfort in our prejudice that the dissipation rate is more intimately related to the shear-containing scales (wavelengths less than 100 m) than the energy-containing scales O($\sim$1000 m). Sensitivity of the observed dissipation rates to the shape of the wavenumber shear spectrum is examined in sections 2b and 4b.

Previous work on the issue of dissipation parameterizations has included the scaling of ϵ with N and shear variance. Gregg and Sanford (1988) suggested that for a constant E internal wave state, ϵ varies as N^2. Gregg (1989), expanding on this study with data at different wave states, showed evidence for an E^2N^2 dependence. However, Gargett (1990) abstracted much of the data in Gregg (1989) from published reports and demonstrated that those data were also consistent with a scaling of $EN^{3/2}$:

> . . . It is demonstrated that . . . (2) the method used by Gregg (1989) to calculate instantaneous wave field energy (*sic*) level E is incorrect and will seriously underestimate E in cases where E is greater than E_{GM}, the energy (*sic*) level of the GM (Garrett and Munk 1975) canonical internal wave field, and (3) the range of variation of E and buoyancy frequency N in the data sets reported by Gregg (1989) is not sufficient to rule out alternative scalings.

The differences between Gregg's and Gargett's scalings bear both on the relevant dynamics connecting the wave field to turbulent production and on predictions for ϵ (and in turn the mixing that occurs) in the abyssal ocean. A major goal of the present work is to determine which (if either) of these scalings is correct.

TABLE 1. Notation for the models and parameters of the GM spectrum

ϵ (W/kg)	Dissipation rate of turbulent kinetic energy
$\hat{E} = b^2 E N_0 N$ (m^2/s^2)	Total energy
F_u	Horizontal velocity spectral density
F_ξ	Displacement spectral density
$F_e = 1/2(F_u + N^2 F_\xi) = b^2 N_0 N E(w, m)$	Vertical wavenumber-frequency energy density
$E(\omega, m) = B(\omega)H(m)E$	Dimensionless energy density
$B(\omega)$	Frequency domain energy density (dimensionless)
$H(m)$	Vertical wavenumber energy density (dimensionless)
E	Dimensionless spectral level
$E_{GM} = 6.3 \times 10^{-5}$	GM specification of E
$b = 1300$ m	Scale height of the thermocline
N	Buoyancy frequency
$N_0 = .00524$ s^{-1}	Reference frequency (3 cph)
$f = 2 \times 7.3 \times 10^{-5}$ sin (lat)	Coriolis parameter
k	Wavenumber vector
x	Position vector
ω	Frequency
m	Vertical wavenumber
$m_* = 3\pi N/bN_0$	Parameter in the GM vertical spectrum
k_h	Horizontal wavenumber
$d\hat{E}/dw$	Frequency domain energy density (Dimensional)
$d\hat{E}/dm = \text{m}^{-2}(S_z + N^2 F_z)$	Vertical wavenumber energy density (Dimensional)
S_z (s^{-2}/cpm)	Vertical wavenumber shear spectral density
F_z (1/cpm)	Vertical wavenumber strain spectral density
$\alpha = (S_z + N^2 F_z)/S_z$	Ratio of HKE + PE to HKE
$\alpha_0 = 4/3$	GM specification of α

Gargett's second point above is simple but bears discussion. Gargett (1990) cites Gargett et al. (1981) and Duda and Cox (1989) [see also Gregg et al. (1993a) and Figs. 2 and 5] as providing evidence that the cutoff wavenumber is independent of N and scales inversely with E, so that $\langle S^2 \rangle = \int_0^{m_c} S_z dm \sim N^2$, and thus Em_c (or $S_z m_c/N^2$) is a constant as illustrated by Fig. 1a. Gregg's (1989) analysis was based on estimates of shear variance determined with a 10-m first difference operator. The first difference estimator yields a biased (underestimated) measure of E in the cases where the half-power point of the first difference transfer function occurs at wavenumbers greater than m_c. The 10-m first difference operator has a half-power point at 0.05 cpm (Polzin 1992) and thus underestimates E in energetic wave fields. Evidence is presented that suggests the bias in Gregg's metric may have masked important discrepancies between the GM-based models and non-GM data in Gregg's (1989) study.

2. Models of dissipation due to internal waves

Before presenting a detailed model–data comparison, the relevant models are briefly reviewed. The model development is based around the GM spectrum (here we employ the GM76 prescription and adjust model results accordingly). In section 2a, dissipation estimates or scalings are determined for GM conditions and for wave fields that retain GM characteristics except for variability in the spectral level (E). Section 2b considers the impact of non-GM spectral characteristics for the dynamical models (i.e., spectral shapes and anisotropy–inhomogeneity).

a. Dissipation parameterizations in GM wave fields

1) McComas and Muller (1981b)

McComas and Muller (1981b, MM in the following) used results from weak resonant interaction theory to produce a dynamical balance for the internal wave field. In that model, the dominance of the parametric subharmonic instability (PSI) at low frequencies ($2f < \omega < 4f$) and large vertical wavenumbers and of the induced diffusion (id) mechanism at high frequencies ($4f < \omega < N$) were used to construct a statistically stationary spectrum in vertical wavenumber space. The resulting solutions closely matched an idealized version of the GM76 spectrum, implying that the sum of the psi and id energy fluxes through wavenumber space was independent of vertical wavenumber in a GM internal wave field. In turn, this energy flux to high vertical wavenumbers may be equated with the turbulent energy dissipation, yielding an estimate of ϵ. Further details can be found in appendix A.

The resulting parameterization is

$$\epsilon = (2.1 \times 10^8 \text{ m}^2) f E^2 N^2. \quad (1)$$

At 32.5°N,

$$\epsilon_{MM}(E_{GM}, N_0) = 1.8 \times 10^{-9} \text{ (W kg}^{-1}\text{)}.$$

2) Henyey, Wright, and Flatté (1986)

A major concern with the resonant interaction theories is the validity of the weak interaction assumption for high frequency and high wavenumber waves (Muller et al. 1986). An alternate approach to the

problem is that of Henyey et al. (1986, hereafter HWF), who described the interactions via an eikonal (ray tracing) approach and calculated the energy fluxes with the help of Monte Carlo simulations of the ray equations. The flow was modeled as a small amplitude test wave propagating in a horizontal background flow. This background was modeled as a Gaussian process consistent with the Munk (1981) version of the GM spectrum.

Henyey et al. determined that their numerical simulations were describable in terms of a simple analytical model in which the energy flux toward high wavenumbers was defined as

$$\left\langle \frac{d\hat{E}}{dt} \right\rangle = \left\langle \frac{d\hat{E}}{dm} \frac{dm}{dt} \right\rangle .$$

The factor $d\hat{E}/dm$ is merely the vertical wavenumber energy density, while the factor dm/dt represents the test wave packet's velocity through vertical wavenumber space. The averaging interval was not specified but is presumably some appropriate volume spanning the internal wave field space–time scales. The energy flux (or equivalently ϵ) was estimated as

$$\left\langle \frac{dE}{dm} \left| \frac{dm}{dt} \right| \right\rangle \frac{1-r}{1+r},$$

where the factor r is the ratio between up- and downscale fluxes. From the numerical simulations, HWF noted that the high vertical wavenumber test wave transports were governed by

$$\frac{dm}{dt} = -\frac{\delta(u\cdot k)}{\delta z} \approx -\frac{\delta u}{\delta z} K_H, \qquad (2)$$

where δ represents partial differentiation, u the background flow, and k the test wave wavenumber vector. The factor $|dm/dt|$ was estimated as $(\langle S^2 \rangle k_h^2 \sqrt{2})^{1/2}$ and assumed to be uncorrelated with the energy spectrum. The factor $\langle S^2 \rangle$ represents the shear variance of the background wave field having vertical wavenumbers smaller than the test wave. After invoking a linear dispersion relation for k_h and rewriting the energy density in terms of the shear and strain (F_z) spectral densities, the model estimate becomes

$$\epsilon(m) = \frac{1}{2} m^{-2}(S_z + N^2 F_z)\left\{ \int_0^m S_z dm \right\}^{1/2} \times m\left\langle \frac{(\omega^2 - f^2)^{1/2}}{(N^2 - \omega^2)^{1/2}} \right\rangle \frac{1}{\sqrt{2}} \frac{1-r(m)}{1+r(m)}. \qquad (3)$$

Note that in general S_z and F_z are functions of m. This representation is identical to that of HWF without invoking the GM formalism. Numerical experiments revealed the test wave spectrum to be in equilibrium with a GM vertical wavenumber spectrum (Flatte et al. 1985), implying stationarity. Guided by the simulations, a value of $r = 0.4$ at $m = 0.2$ cpm was chosen. Although HWF do not describe their analysis as such, the factor in (3) involving wave frequency was effectively estimated as the expected value from the GM frequency spectrum. Extrapolation of the model to higher spectral levels explicitly assumed that the ratio between up and down wavenumber energy fluxes $r(m)$ was solely dependent on the rms shear contained in waves of larger scale.

To more efficiently test the models, the HWF prediction is converted here to GM76 spectral levels. The conversion only alters the magnitude of the model estimate for the dissipation rate and is discussed in Appendix A. Identical conclusions are reached regardless of which spectral representation is employed (Polzin 1992). For GM76 the model estimate becomes

$$\epsilon \,(\mathrm{W\ kg^{-1}}) = (1.9 \times 10^7\ \mathrm{m^2}) f E_{\mathrm{GM}}^2 N^2 \cosh^{-1}\left(\frac{N}{f}\right). \qquad (4)$$

At 32.5°N,

$$\epsilon_{\mathrm{HWF}}(E_{\mathrm{GM}}, N_0) = 7.9 \times 10^{-10}\ (\mathrm{W\ kg^{-1}}).$$

3) GARGETT AND HOLLOWAY (1984)

Much of the observational dissipation data preceding Gargett and Holloway (1984 GH) suggested an inverse buoyancy scaling of ϵ/N^2; that is, $K_\rho = 0.25\epsilon/N^2$ (Osborn 1980; Oakey 1982) increasing with depth as N decreased. As little or no information about the internal wave field was reported with those microstructure data, GH took as a starting point that the finescale spectral levels were roughly consistent with the GM model. In explaining the apparent inverse scaling of ϵN^2 with N, GH avoided the classical Reynolds decomposition of the kinetic energy equation, balancing dissipation with the vertical divergence of the energy flux; that is,

$$-\epsilon \sim \left\langle uw\left(\frac{du}{dz}\right)\right\rangle = C_1\left\langle u^2 w^2 \left(\frac{du}{dz}\right)^2 \right\rangle^{1/2},$$

where C_1 is a triple correlation coefficient (suggested to be independent of N). Gargett and Holloway went on to assert that internal wavelike motions determine the variances in the energy equation and assumed that these motions retain their nominal internal wave (E, N) scalings. For a single wave, GH inferred a scaling of $\epsilon \sim EN^1$ (Gargett 1990). For a multiwave (GM) environment, Gargett (1990) suggested a scaling of

$$\epsilon \sim EN^{3/2}. \qquad (5)$$

4) MUNK (1981)

The Munk (1981) model links the time rate of change of internal wave energy to the rate of occurrence of instabilities: $d\hat{E}/dt = -\sigma \hat{E} p(\phi > 1)$. Here σ is the frequency of occurrence per unit time of a dissipation

event, $\hat{E}$ is the energy of the internal wave field, and $p(\phi > 1)$ represents the probability of an instability criterion being exceeded. Gaussian statistics are assumed for ϕ: $p(\phi > 1) = (2\langle\phi^2\rangle/\pi)^{1/2} \exp[-1/(2\langle\phi^2\rangle)]$. For shear instability, $\phi = (4N^2/S^2)^{-1/2}$. The timescale is taken to be the fastest available: that of the strain field, $\sigma = \sqrt{f}N/\pi$. The resulting scaling for ϵ is $f^{1/2}N^{3/2} \times E^{3/2} \exp(-\text{const}/E)$ if the cutoff wavenumber is taken to be independent of E (Gregg 1989). Dissipations quoted for this model by Gregg (1989) are much greater than those of the preceding models; at $N = 3$ cph, $\epsilon = 1.3 \times 10^{-8}$ W kg^{-1}. Furthermore, the exponential scaling of E yields dissipation predictions that are much too large at high E (Gregg 1989; Gargett 1990). This dependence is reduced significantly if the variation in the high wavenumber cutoff with E is taken into account. For spectral levels greater than GM (for which the cutoff occurs at wavenumbers smaller than 0.1 cpm), evaluation of the shear variance by integrating the canonical spectrum out to 0.1 cpm produces

$$\langle\phi^2\rangle = 0.7\left(1 + \ln\left(\frac{E}{E_{GM}}\right)\Big/4\right).$$

The expression for ϵ then becomes

$$\epsilon = -\frac{d\hat{E}}{dt} = \hat{E}\frac{(fN)^{1/2}}{\pi}\left(0.7\left(1 + \ln\left(\frac{E}{E_{GM}}\right)\right)\Big/2\pi\right)^{1/2} \times \exp\left\{-2/0.7\left(1 + \ln\left(\frac{E}{E_{GM}}\right)\right)\right\}. \quad (6)$$

For $E/E_{GM} > 2$, the scaling of this expression is approximately $f^{1/2}N^{3/2}E^2$.

b. *Dissipation parameterizations in non-GM wave fields*

The dynamical models discussed in section 2a equate the dissipation rate with the energy flux through the vertical wavenumber spectrum due to internal wave–wave interactions under the proviso that the model spectrum, which forms the basis for the analysis, is statistically stationary with respect to the nonlinear interactions. The models (MM and HWF) do indicate that the GM vertical wavenumber spectrum is statistically stationary. Non-GM spectral characteristics potentially invalidate the stationarity criterion. A nonstationary vertical wavenumber spectrum implies convergence or divergence of energy in wavenumber space, and thus the energy flux at arbitrary wavenumber may not necessarily equal the dissipation rate. In this section, the impact of non-GM spectral characteristics on the net up-wavenumber energy flux are considered.

The non-GM spectral characteristics discussed below include variations in wavenumber–frequency spectral shapes and the twin issues of anisotropy and inhomogeneity. The effects of variations in spectral shapes have been discussed in Henyey (1991) for the induced diffusion mechanism and the Eikonal approach of HWF. We refine those results below. With regard to the issue of the net up-wavenumber energy flux at small scales, anisotropy and inhomogeneity have not been formally evaluated in the context of either dynamical model. Below we argue that these issues are not of primary importance. However, these arguments are in need of theoretical verification.

The entire range of non-GM conditions is not considered. We have interpreted our measurements of shear and strain in terms of linear internal wave kinematics. There is not sufficient information in these data to distinguish between the vortical mode and internal wave motions (e.g., Kunze and Sanford 1993; Kunze 1993). Any effects associated with finite-amplitude wave packets (e.g., changes in the dispersion relation associated with solitary wave behavior) are not considered for similar reasons.

The GM model assumes the wavenumber and frequency spectra to be separable, implying

$$S_z + N^2F_z = \alpha S_z. \quad (7)$$

[The factor α is related to the shear-strain ratio R_w, section 3, by $R_w = 1/(\alpha - 1)$.] Results from both dynamical models indicate that the equilibrium frequency spectrum (with respect to either wave interaction mechanism) is nonseparable. Since the condition of nonseparability cannot be interpreted within the context of this study, we have not used separability as a criterion to differentiate datasets. Corrections associated with deviations from the equilibrium spectrum could be developed if the equilibrium spectrum were defined.

1) WAVENUMBER SPECTRAL SHAPES

Prior to considering the implications of spectral deviations for the model results, extensions to the canonical spectrum of Gargett et al. (1981) need to be considered. Gargett et al. (1981) discussed a vertical wavenumber spectrum (S_z) that was white at low wavenumber and then fell as m^{-1} beyond a point where the shear variance ($\int_0^{m_c} S_z dm$) exceeded γN^2 (Fig. 1a). (In Gargett et al., $\gamma = 1$; here we use the value $\gamma = 0.7$ from GM76.) Scaling the ordinate of shear spectra having this general shape by $1/EN^2$ and the abscissa by E does indeed collapse the spectra in the high wavenumber ($m > m_c$) regime. If, however, the shear spectrum obeys a power law [e.g., $S_z \sim (m/m_c)^p$] for wavenumbers smaller than m_c, this scaling does not in general collapse the high wavenumber regime (Fig. 1b). To the extent that the above (E, N) scaling is observed to collapse the high wavenumber regime (Fig. 5), this implies that such a simple model shear spectrum is inappropriate. In the following derivations we consider a family of spectral shapes that exhibits a low wavenumber power law [$S_z \sim (m/m_c)^p$] and a high wave-

number m^{-1} regime, which either contains or can be extrapolated to the point $(m, S_z) = (0.1 \text{ cpm}, S_{z\text{GM}})$ (Fig. 1c).

(i) *HWF*

The test wave vertical wavenumber spectrum of HWF agreed quite well with the GM spectrum, implying that this spectrum is statistically stationary with respect to the interaction mechanisms. The impact of deviations from GM spectral shapes upon the dissipation rate in the HWF model can be assessed if one assumes the ratio between the up and down wavenumber fluxes (r) is a function only of the rms shear in waves of larger scale; that is; $r(m_c)$ is constant (HWF; Henyey 1991) and evaluates the expression for the dissipation rate at m_c [Eq. (3)]. One needs to distinguish between positive and negative low wavenumber slopes (p). For $p > 0$, Eq. (3) becomes

$$\epsilon = \frac{1}{2} m_c^{-1} \alpha S_z(m_c) \gamma N^2 \times \left\langle \left[\frac{(\omega^2 - f^2)}{(N^2 - \omega^2)} \right]^{1/2} \right\rangle \frac{1}{\sqrt{2}} \frac{1 - r(m_c)}{1 + r(m_c)}.$$

Since $S_z(m_c)$ is universal (Fig. 1c), the up-wavenumber energy flux is unaffected. If $p < 0$ and the form

$$S_z = \frac{\gamma N^2 (p + 1)}{m_c} \left(\frac{m}{m_c} \right)^p$$

is assumed, Eq. (3) reduces to

$$\epsilon(m_c) = \frac{\alpha \gamma^{3/2} N^3}{2} \frac{(p + 1)}{m_c^2} \times \left\langle \left(\frac{\omega^2 - f^2}{N^2 - \omega^2} \right)^{1/2} \right\rangle \frac{1}{\sqrt{2}} \frac{1 - r(m_c)}{1 + r(m_c)}. \quad (8)$$

Thus a scaling of $\epsilon \sim (p + 1)$ is expected.

(ii) *MM*

The results of a numerical model that included all interacting triads suggested that the GM vertical wavenumber spectrum is stationary. Corrections for non-GM low wavenumber spectral slopes in the MM model can be derived by considering the psi mechanism. In that model, the dissipation rate was equated with the sum of the "psi" and "id" energy fluxes: $\epsilon = \hat{Q}_{\text{psi}} + \hat{Q}_{\text{id}}$. If an ω^{-2} frequency power spectrum is assumed, the psi flux at m_c can be rewritten as (appendix A)

$$\hat{Q}_{\text{psi}} \sim f N^2 \alpha S_z(x m_c) S_z(m_c), \quad (9)$$

where $x = \sqrt{10}$. As before, two cases can be distinguished. For $p > 0$, S_z is universal for wavenumbers $\geq m_c$ (Fig. 1c) and the energy fluxes are unaffected. For $-0.45 < p < 0$ and if the spectral form

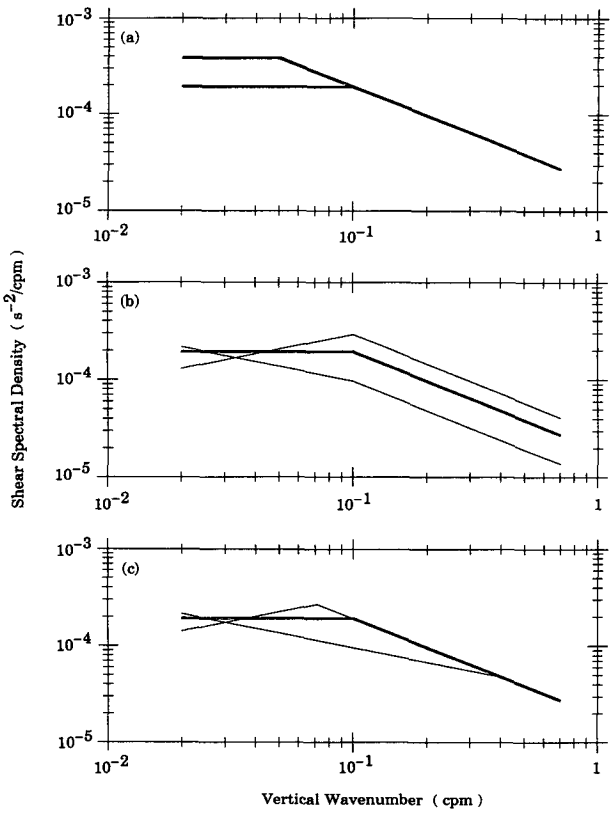

FIG. 1. Models for the shear spectrum. (a) The canonical shear spectrum of Gargett et al. (1981); S_z is white at low wavenumber, then falls as m^{-1} at a wavenumber m_c defined by $\int_0^{m_c} S_z dm \sim N^2$. (b) A constant low wavenumber slope with a transition to an m^{-1} form at m_c. (c) The cutoff wavenumber m_c and the transition point differ so that the high wavenumber regime is universal. Model spectra (a) and (c) are employed here.

$$S_z = \frac{\gamma N^2 (p + 1)}{m_c} \left(\frac{m}{m_c} \right)^p$$

is assumed as before, then

$$\hat{Q}_{\text{psi}} \sim f N^2 \alpha (p + 1)/m_c^2,$$

since $S_z(x m_c)$ is universal (Fig. 1c). As with the HWF revision a $(p + 1)$ scaling is deduced.

The results of our power-law analysis differ from that of Henyey (1991). For both the MM and HWF constructs, Henyey argued from the approximations $\langle S^2 \rangle \sim m S_z$ and $1/m_c \sim \langle S_{10}^2 \rangle$ to obtain $\epsilon \sim S_{10}^{4/(p+1)}$, where S_{10} represents a 10-m first difference shear. This and the present derivations are equivalent if shear spectra exhibit a constant spectral form to 0.1 cpm. In practice however, shear spectra exhibiting positive slopes and those with spectral levels greater than the GM specification roll off before 0.1 cpm, and the Henyey derivation suffers from the same criticisms that Gargett (1990) made of Gregg (1989).

Revisions to both models suggest that for the range of observed vertical wavenumber slopes (section 4,

TABLE 2. Scaling parameters for the TOPO—Deep data. Energy levels are presented in a nondimensional form by dividing the average shear spectral density by its GM76 specification (13). Dissipations are presented in the form of eddy diffusivities, $0.25\epsilon/N^2$. The shear and strain ratio [R_ω, Eq. (14)] is followed by the derived estimates involving frequency content [Eqs. (15) and (16)]. An estimate of the slope of the vertical wavenumbers spectrum for wavenumbers less than m_c required in section 4b is included with an estimate of the standard error. Slope estimates immediately followed by an asterisk excluded the lowest wavenumber in the spectrum.

Bin	Depth range (db)	N^2/s^{-2}	$K_\rho \times 10^{-4}$ ($m^2\ s^{-1}$)	E_1	R_ω	$\frac{\langle\omega\rangle}{f}$	$\frac{N}{f}\left\langle\frac{k_h}{m}\right\rangle$	Spectral slope	Piece length (db)	Number of pieces	Number of profiles
TD1	100–200	1.20×10^{-4}	0.099	1.49	4.61	1.25	0.74	−.17* ± .25	128	1	8
TD2	200–400	3.51×10^{-5}	0.069	1.46	5.60	1.20	0.66	−.27 ± .07	128	2	8
TD3	400–1000	1.05×10^{-5}	0.15	1.71	4.88	1.23	0.72	−.09 ± .11	128	6	8
TD4	1000–1500	4.15×10^{-6}	0.097	1.96	7.52	1.14	0.55	−.06 ± .11	128	5	8
TD5	1500–2000	2.53×10^{-6}	0.131	1.99	5.65	1.20	0.66	−.09 ± .10	128	5	8
TD6	2000–2500	1.41×10^{-6}	0.098	1.78	4.94	1.23	0.71	−.12 ± .09	256	2	5
TD7	2500–3000	8.59×10^{-7}	0.160	2.48	5.74	1.16	0.65	−.12 ± .11	256	2	5

Tables 2 and 3) inclusion of the spectral slope corrections changes the predicted dissipations by at most a factor of 2. Moreover, the observations discussed in section 4b bring these scalings into question as wavenumber slopes are not obviously related to variability in the observed dissipations. Wavenumber slope scalings will therefore be neglected in the theoretical developments that follow.

2) FREQUENCY SPECTRAL SHAPES

(i) *HWF*

Action flux vectors are presented in HWF. These reveal an up-wavenumber, up-frequency flow up until 0.05 cpm. At higher wavenumbers the flow has reduced change in frequency. This suggests that the GM frequency spectrum is not in equilibrium with the wave–wave interactions. In turn, this implies the equilibrium spectrum is nonseparable.

Within the context of the Monte Carlo simulations of the HWF model, individual test waves interact with the background at a rate proportional to

$$\left[\frac{(\omega^2 - f^2)}{(N^2 - \omega^2)}\right]^{1/2}.$$

Since the net up-wavenumber energy flux is formed as a weighted sum over the test wave field, determining the frequency scaling of the dissipation rate for a non-GM field involves ascertaining the expected value of the frequency within the test wave field from the frequency spectrum:

$$\left\langle\left(\frac{\omega^2 - f^2}{N^2 - \omega^2}\right)^{1/2}\right\rangle = \int_f^N \left(\frac{\omega^2 - f^2}{N^2 - \omega^2}\right)^{1/2} \frac{d\hat{E}}{dw}\, dw \Big/ \int_f^N \frac{d\hat{E}}{dw}\, dw. \quad (10)$$

TABLE 3. Scaling parameters for the TOPO_Deep profiles exhibiting heightened spectral levels (TD6U and 7U), the TOPO_F (F1–F3), WRINCLE (W1–W4), and NATRE (N1–N6) datasets. The presentation is similar to that for Table 2.

Bin	Depth range (db)	N^2/s^{-2}	$K_\rho \times 10^{-4}$ ($m^2\ s^{-1}$)	E_1	R_ω	$\frac{\langle\omega\rangle}{f}$	$\frac{N}{f}\left\langle\frac{k_h}{m}\right\rangle$	Spectral slope	Piece length (db)	Number of Pieces	Number of Profiles
TD6U	2000–2500	1.41×10^{-6}	0.34	3.73	8.13	1.13	0.53	.26 ± .18	256	2	3
TD7U	2500–3000	8.59×10^{-7}	1.54	8.76	6.94	1.16	0.58	.43 ± .60	256	2	3
F1	700–900	8.86×10^{-6}	0.86	4.18	4.81	1.24	0.72	.48 ± .10	256	1	15
F2	900–1100	6.11×10^{-6}	0.67	2.65	3.55	1.34	0.89	.22 ± .12	256	1	15
F3	1100–1300	4.19×10^{-6}	1.24	2.43	2.19	1.63	1.29	.01 ± .12	256	1	15
W1	400–600	2.63×10^{-5}	0.84	4.63	9.91	1.11	0.47	.47 ± .28	256	1	10
W2	400–600	2.62×10^{-5}	0.68	6.42	17.0	1.06	0.35	.90 ± .53	256	1	10
W3	400–600	2.62×10^{-5}	1.19	7.16	10.4	1.10	0.46	.15 ± .62	256	1	10
W4	400–600	2.67×10^{-5}	0.76	4.55	6.98	1.16	0.58	−.39* ± .24	256	1	10
N1	250–500	1.58×10^{-5}	0.25	1.88	4.81	1.24	0.72	−.59* ± .10	256	1	10
N2	500–1000	1.13×10^{-5}	0.12	2.02	4.63	1.25	0.74	−.41* ± .05	512	1	10
N3	1000–1500	5.67×10^{-6}	0.20	2.45	5.11	1.22	0.70	−.59* ± .08	512	1	10
N4	1500–2000	2.57×10^{-6}	0.18	2.70	4.62	1.25	0.74	−.43* ± .12	512	1	10
N5	2000–2500	1.48×10^{-6}	0.34	4.09	6.92	1.16	0.58	−.46 ± .10	512	1	10
N6	2500–3000	9.35×10^{-7}	0.44	4.81	10.3	1.10	0.46	−.45 ± .15	512	1	10

The resulting parameterization for the HWF model becomes

$$\epsilon = 7.9 \times 10^{-10} \frac{f}{f_0} \frac{N^2}{N_0^2} \left(\frac{0.1 \text{ cpm}}{m_c} \right)^2 \frac{\alpha}{\alpha_0} \frac{N}{f} \times \left\langle \left(\frac{\omega^2 - f^2}{N^2 - \omega^2} \right)^{1/2} \right\rangle (\text{W kg}^{-1}). \quad (11)$$

(ii) *MM*

One shortcoming of the analytic model described by MM was the lack of a stationary frequency spectrum. Both the psi and id mechanisms transfer energy into inertial frequencies. Moreover, the inertial peak in the GM spectrum is not sufficiently pronounced to be in equilibrium with the psi mechanism (Muller et al. 1986). This effect must be balanced by nonidentified interactions in order for the frequency spectrum to be stationary. The results of a numerical model that includes all the interacting triads suggests that the equilibrium frequency spectrum is also nonseparable. The analytic model is most directly concerned with the high frequency wave field, and revisions to that model will be appropriately limited. Corrections for non-GM frequency spectra were derived in Henyey (1991) through an approximation to the transport integral in the induced diffusion limit. It was determined that individual waves "diffuse" at a rate linearly proportional to their frequency, implying that wave fields containing a disproportionate number of high frequency constituents will have larger than average up-wavenumber fluxes (and hence larger dissipation rates). The resulting parameterization is therefore (with $p = 0$)

$$\epsilon = 1.79 \times 10^{-9} \frac{f}{f_0} \frac{N^2}{N_0^2} \left(\frac{0.1 \text{ cpm}}{m_c} \right)^2 \frac{\alpha}{\alpha_0} \times \frac{\langle \omega/f \rangle}{\langle \omega/f \rangle_{\text{GM}}} (\text{W/kg}). \quad (12)$$

In both dynamical models the sensitivity to wave frequency derives from the larger group velocities for high-frequency waves; higher group velocity implies higher encounter rates with other internal waves. The scale analysis for the weak interaction limit is in some sense incomplete as both the psi and id mechanisms are not considered simultaneously.

3) INHOMOGENEITY AND ANISOTROPY

(i) *MM*

McComas and Muller (1981a) summarize the mechanisms that dominate the spectral transfers under the weak interaction approximation. One of these, termed "elastic scattering," acts to equalize the energy between upward and downward propagating high frequency waves with similar vertical wavelengths. The process is facilitated by the presence of a low-frequency wave of half the vertical wavelength. McComas and Muller (1981a) state that the energy exchanges within the triad act primarily to equalize the energy content of the high frequency waves and that little energy gets fluxed to smaller scales. With little net up-wavenumber energy flux, it follows that anisotropic conditions should not have a large impact upon dissipation rates. Numerical simulations appear to suggest that this is the case, but the vertical wavenumber energy fluxes were not compared. Corresponding theoretical results do not exist for inhomogeneity. The resonance condition implies that two waves of similar frequency and horizontal wavenumber (oppositely signed) interact with a nonhydrostatic wave of one-half the horizontal wavelength. Unfortunately, the theoretical basis for McComas and Muller (1981a) invokes the hydrostatic approximation.

(ii) *HWF*

Concerns about the effects of anisotropy and inhomogeneity upon the average energy fluxes predicted by the HWF model are straightforwardly addressed. The eikonal relationship of this model is neither modified nor altered in a unidirectional background field. The isotropic simulations contain both critical layers and turning points (Flatté et al. 1985; Henyey and Pomphrey 1983); anisotropic simulations should not differ in this regard. We believe the relevant question to be the following. Given a unidirectional (but yet stochastic) background field, do test waves propagating against the background evolve at different rates on average than those propagating with the background? Given the eikonal equation above [Eq. (2)] and the stochastic representation of the background, we fail to see how, on average, this is possible; the net up-wavenumber energy fluxes should not depend upon the directionality of the background field. We would, of course, like to see this verified.

3. Data and analysis techniques

a. Data

All data in this study were obtained with the High Resolution Profiler (HRP) (Schmitt et al. 1988), a free-falling, internally recording profiler. The HRP is equipped with an acoustic velocimeter that senses relative horizontal flow. Estimates of the oceanic velocity profile are deduced from these relative velocity data and onboard accelerometer and magnetometer measurements using a variation of the point mass model of Hayes et al. (1984). Temperature, conductivity, and pressure are sensed with an NBIS Mark III CTD, calibrated at the Woods Hole Oceanographic Institution Facility with reference to historical deep-water temperature–salinity relationships. Time series of velocity, temperature, and conductivity data obtained during

profiler descent were binned into 0.5-dbar pressure intervals and averaged. (Note that for convenience throughout we use "m" and "dbar" interchangeably.) Further details can be found in Schmitt et al. (1988).

Dissipation estimates were created by averaging two components of shear variance at centimeter scales and assuming (3D) isotropy (Yamazaki and Osborn 1990). Velocity microstructure was sensed with airfoil probes (Osborn 1974) whose calibrations were determined in the Bedford Institute of Oceanography facility operated by N. Oakey. Shear variance was estimated in the frequency domain within 0.5-dbar intervals aligned with the finescale profiles. Gradient variances were calculated after spectrally transforming and applying spectral corrections for electronic and sensor transfer functions by integrating periodograms out to a relative minimum, beyond which vibration noise dominates the signal. The microstructure processing algorithms are based upon those developed by N. Oakey (1990, personal communication). Further details about this particular application can be found in Polzin and Montgomery (1995).

Calibration uncertainty and measurement error combined yield errors for one-component shear variance estimates as large as 50%. The assumption of isotropy may cause dissipation values to be overestimated by a factor of 2 (Itsweire et al. 1993). Noise levels are equated with dissipation values where the shear spectrum departs significantly from Naysmith's (1970; Oakey 1982) empirical form. For the present data, this occurs about $\epsilon_n \sim 1 \times 10^{-11}$ W kg^{-1}. The statistical uncertainty of averaged dissipation rate estimates are derived with a bootstrap technique described below.

The question of buoyancy scaling is addressed first (section 4a) by analyzing a subset of data obtained in March 1991 that exhibited GM internal wave characteristics and spanned a large range in N. Eight profiles (collectively referred to here as TOPO_Deep) extending to 3000-m depth in the vicinity of Fieberling Guyot in the eastern North Pacific Ocean (32.5°N,128°W) were selected. These profiles were taken at a distance of 20–40 km from the center of the Guyot in 3400–4000 m of water. Of these eight profiles, three (located near the base of the seamount) exhibited heightened internal wave spectral levels and turbulent dissipation below 2000 m. The 2000–3000-m segments of these profiles are treated separately below. The seamount is located sufficiently far from the coast (1000 km west of southern California) as to be outside the range of influence of the California Current. Large-scale background flows were observed to be less than 2 cm s^{-1} at the time of the experiment (K. Brink 1993, personal communication).

Datasets exhibiting non-GM characteristics included a set of 15 profiles from the steep flank of Fieberling Guyot (here designated TOPO_F), the three deep segments noted above, a set of 40 profiles from the center of a warm core ring obtained during the Warm Ring Inertial Critical Layer Experiment (WRINCLE), and a set of 10 profiles from a midocean regime [North Atlantic Tracer Release Experiment (NATRE)].

The TOPO_F profiles consist of two time series of 24-hours duration with a nominal sampling interval of 3 hours. The time series, separated by 13 days, were conducted in water depth of approximately 1500 m where the local bottom slope approached 0.5. We utilize data to 1300 m (a level sampled by all of the HRP deployments). Anomalous wave fields have been observed previously in the vicinity of topographic features (e.g., Wunsch and Webb 1979; Eriksen 1982; Kunze et al. 1992). Internal waves reflecting from a sloping boundary tend to reflect into small wavelengths (Eriksen 1985), resulting in heightened shear levels. Enhanced small-scale shear levels may also be noted if waves generated by a background flow or barotropic tidal flow over topography (Bell 1975) have characteristically small vertical wavelengths.

The WRINCLE dataset was obtained in March–April of 1990 from a warm core ring of the Gulf Stream (40°N,64°W). The ring's radius was approximately 50 km; the profiles analyzed here were obtained within 40 km of ring center below the core of near-solid body rotation. The WRINCLE profiles extended to 1000-m depth; we focus here on observations between 372 and 628 m in which N was relatively constant. The relative vorticity at this level was small, approximately $0.1f$ (Kunze et al. 1995), and is ignored here. The 40 HRP profiles were subdivided equally into four groups, representing different time periods during the cruise and were analyzed separately. Heightened internal wave spectral levels are characteristic of warm core rings [e.g., Kunze (1986)], presumably due to more efficient wave generation processes [e.g., Rubenstein and Roberts 1986] and/or trapping within a ring's vorticity bowl of surface-generated waves having frequencies below the Coriolis (planetary) frequency (Kunze 1985; Kunze et al. 1995).

The third dataset (NATRE) was obtained in April of 1992 west of the Canary Islands in the vicinity of 26°N, 29°W. The 10 profiles examined here, extending to 3000 m, comprise a N–S section approximately 400 km in length. This region has previously been shown to exhibit a large amplitude, semidiurnal tide (Rossby 1988; Siedler and Paul 1991). Spatial sampling during this cruise revealed a weak mesoscale eddy field: gradients in the dynamic height field at 300 db relative to 1500 db implied geostrophic velocities of order 5–15 cm s^{-1}.

The three cruises represent distinct geographic/oceanographic regimes. Note, however, that a bias toward midlatitudes and late winter/early spring conditions exists.

b. *Analysis techniques*

The models discussed in section 2 require the estimation of average buoyancy frequencies, shear and

strain spectral levels, and the cutoff wavenumber of the shear spectrum. The procedures for estimating these parameters are briefly discussed here. Further details relating to data processing can be found in Polzin (1992, appendix A) and in Schmitt et al. (1988).

For each dataset, the water column was subdivided into depth bins, each having approximately constant buoyancy frequency, column 2 of Tables 2 and 3. (Constant N is most problematic for the TOPO_Deep interval of 200–400 m within which N varies by a factor of 2. While our conclusions do not hinge critically on data from this bin, consistent model–data relationships are in fact found at this depth as well.) The N profile was estimated for these sets from ensemble average profiles of temperature and salinity on pressure surfaces using the adiabatic leveling method (Bray and Fofonoff 1981). The 8 TOPO_Deep, 15 TOPO_F, and 10 NATRE profiles were separately averaged to obtain the background stratification profiles for these respective datasets. For the WRINCLE data, averaged temperature and salinity profiles were created from those profiles nearest ring center. Thirty-seven of the 40 profiles were represented in this average.

Within each depth bin of each set of profiles, overlapping data piece lengths were selected (128, 256, or 512 m) in which to Fourier transform the profiles (column 10 of Tables 2 and 3). The smaller value was generally chosen to limit variability in N within the transform intervals. For highly energetic regions, or for shear spectra exhibiting negative slopes with vertical wavenumber (red shear spectra), a larger interval was chosen. Employing a variable bandwidth allows for more robust estimates of the average spectral level over those parts of the spectrum that contribute significantly to the shear variance. Within each depth bin, a single length was employed. (Spectra with different elementary bandwidths were not averaged together). The spectra were overlapped as evenly as possible: for example, a spectrum nominally from 1500 to 1600 db started at 1486 db and ended at 1614 db. The appropriate mean N profile from above was taken to estimate the average buoyancy frequency over each piece length of the analysis, $\hat{N}$.

Velocity components within each transform depth interval were buoyancy scaled by multiplying by $N_0/\hat{N}$ with $N_0 = 3$ cph. This normalization accounts for the N^2 scaling of S_z and is consistent with the WKB approximation. The scaled velocity profiles were detrended with a curve determined from a linear least-squares fit since wavelengths larger than the interval in question are not well represented by the transform. Spectral leakage was limited by applying 10% cosine tapers and prewhitening by first differencing before transforming. (Details of the detrending and windowing procedures do not affect our results; tests estimating shear variance with and without the least-square fitting and tapering, for example, differed by 1%.) After Fourier transforming, the resulting coefficients were "recolored" to correct for the first difference operator and normalized to correct for the loss of variance associated with the tapering operation. The Fourier coefficients representing the orthogonal velocity components were then squared, multiplied by squared wavenumber, and averaged. Depth bin/set averaged shear spectra, normalized to 3 cph, were constructed by averaging coefficients of the available shear periodograms within each ensemble.

As noted in the introduction, internal wave shear spectral levels were estimated for wavenumbers less than the cutoff vertical wavenumber. An average shear spectral density,

$$S_{z0} = \frac{1}{m_c}\int_0^{m_c} S_z\,dm = \frac{\gamma N_0^2}{m_c} = \frac{0.1 \text{ cpm } S_{z\text{GM}}}{m_c},$$

can be obtained from the definition of the cutoff wavenumber. Rather than making subjective estimates of where in vertical wavenumber average spectra changed from flat to m^{-1} behavior, we employed a variance criteria. Buoyancy-scaled shear spectral density estimates were integrated in wavenumber to the point where the shear variance exceeded $0.7N_0^2$ (which defines m_c). The variance was subsequently divided by the bandwidth of the estimate giving the average shear spectral level for wavenumbers less than m_c. This upper limit of integration was chosen on the basis of the GM76 spectra:

$$\int_0^{0.1 \text{ cpm}} S_{z\text{GM}}\,dm = 0.7N_0^2$$

(see appendix A).

For input to the model dissipation prediction expressions, we employ the nondimensional spectral level E_1, or equivalently, 0.1 cpm/m_c:

$$E_1 = \frac{S_{z0}}{S_{z\text{GM}}} = \frac{0.1 \text{ cpm}}{m_c}. \tag{13}$$

Therefore, E_1 can be interpreted as either a measure of the spectral level or the cutoff wavenumber itself. This dual definition has important consequences for this study. If the observed low-wavenumber spectral shape deviates from the GM specification in the form of a power-law subrange, consistent corrections to the model expressions for dissipation rate can easily be accommodated by estimating the slope of the wavenumber spectrum (section 2b).

The averaged temperature and salinity profiles were also used to create mean potential density profiles. Profiles of internal wave vertical displacements were estimated from the difference in pressure of constant potential density surfaces between the individual and averaged profiles. The profiles of vertical displacement were then spectrally transformed in the same manner as the velocity profiles to produce set- and bin-averaged strain spectra. (Strain is the vertical derivative of the vertical displacement.) A set- and bin-averaged strain

spectral density F_{z0}, the equivalent of S_{z0}, was defined by integrating the set- and bin-averaged strain spectra out to m_c (defined by S_z) and then dividing by the bandwidth of the estimate. Ideally, this analysis should be conducted with time series data to minimize interpretation of baroclinic gradients as wave displacements and limit the possible effects of finestructure contamination, but this was not always possible. The TOPO_Deep and NATRE average potential density profiles represent a spatial average, while the WRINCLE average potential density profile is a mixed space–time average. We do not believe spatial gradients or density finestructure significantly affected the present strain estimates.

Noise associated with the salinity calculation at depth required the strain spectra to be estimated from potential temperature for the TOPO_Deep profiles below 2500 db. Potential temperature profiles were demeaned, detrended, and normalized by the mean vertical potential temperature gradient calculated over each transform interval to obtain displacement profiles. No intrusions were observed at these depths, so temperature was a good proxy for density. Processing then followed that above.

The model dissipation expressions involve factors containing wave frequency. For a single wave in the absence of mean flow, it is straightforward to derive an expression for the ratio of the internal wave shear (S_z) and strain (F_z) spectra:

$$\frac{S_z}{N^2 F_z} = \frac{(\omega^2 + f^2)(N^2 - \omega^2)}{N^2(\omega^2 - f^2)} = R_\omega. \quad (14)$$

Kunze et al. (1990) were the first to exploit the shear-to-strain ratio to deduce wave frequency; it follows directly from Fofonoff (1969), since the shear to strain ratio is identical to the ratio of horizontal kinetic energy to potential energy. For the GM spectrum, $R_\omega = 3$. It is not apparent that this represents an appropriate estimate of the frequency content in a multiple wave field. As argued above, we suggest use of the spectrally weighted frequency within the wave band (10). Lacking temporal measurements, the factors involving frequency content are estimated here from the average spectral densities S_{z0} and F_{z0}. The squared frequency is calculated by solving the quadratic represented in (14):

$$\omega^2 = (N^2(1 - R_\omega) - f^2 + (N^4(R_\omega - 1)^2 + 2N^2 f^2(1 + 3R_\omega) + f^4)^{1/2})/2. \quad (15)$$

The wave frequency correction to the MM model is estimated as the square root of the above expression. The ratio between horizontal and vertical wavenumbers required for the wave frequency correction to the HWF model (11) is determined from a similar quadratic equation:

$$\frac{k_h^2}{m^2} = \frac{(\omega^2 - f^2)}{(N^2 - \omega^2)} = \left\{ -R_\omega + 1 + \frac{f^2}{N^2} + \left[\left(R_\omega - 1 - \frac{f^2}{N^2} \right)^2 + 8R_\omega \frac{f^2}{N^2} \right]^{1/2} \right\} \Big/ 2R_\omega. \quad (16)$$

Note that the above expressions (15) and (16) are not identical to the expected values [e.g., (10)]. For the GM spectrum, the expected values of Nk_h/fm and ω/f are $2\pi \cosh^{-1}(N/f)$, whereas use of the shear–strain ratio for GM specifications ($R_\omega = 3$) leads to $k_h/m = f/N$ and $\omega = \sqrt{2}f$. The consistency of these estimates is examined in detail in appendix B. This analysis suggests that more accurate estimation of the expected values of the wave-frequency corrections would significantly improve the model dissipation estimates in the non-GM model/data comparison of section 4.

Use of the average spectral densities to estimate R_ω implicitly assumes the wavenumber–frequency spectra to be separable. A strict interpretation of the dynamical models suggests the use of the shear strain ratio at the cutoff wavenumber m_c. A spectrally averaged estimate of the ratio has been employed in this study since, in general, the statistical uncertainty associated with the ratio between shear and strain spectral densities for a single wavenumber is large. The issue of separability is examined below through the vertical wavenumber dependence of the shear/strain ratio. For red displacement spectra the semi-Lagrangian transformation does not redistribute variance in vertical wavenumber (Anderson 1992). Since these vertical profile measurements effectively integrate over all frequencies, shear–strain ratio statistics presented here do not distinguish between Eulerian and semi-Lagrangian interpretations.

Dissipations are presented in the form of inferred eddy diffusivities; that is,

$$K_\rho = \frac{R_f}{1 - R_f} \frac{\epsilon}{N^2}$$

(Osborn 1980), with a fixed value of flux Richardson number $R_f = 0.20$ (Oakey 1982). As will be seen, this quantity is more statistically stationary with depth than ϵ. Variation of R_f and the efficiency of the turbulent mixing is not examined here. (Indeed, we expect that the mixing efficiency will exhibit a Reynolds number dependence, where the Reynolds number is that appropriate for the outer scales of the turbulence.) In general, a length scale of 20 m was employed to estimate the N^2 required in the inferred diffusivity calculation except in the case of the TOPO_Deep profiles below 2000 db. For these data, a length scale of 50 m was dictated by the presence of highly energetic finestructure adjacent to the seamount. Additionally, it was required that N^2 be greater than the square of the buoyancy frequency corresponding to four times the least bit in the temperature measurement. If this condition was not met, the length scale of the least-squares estimate of N^2 was doubled.

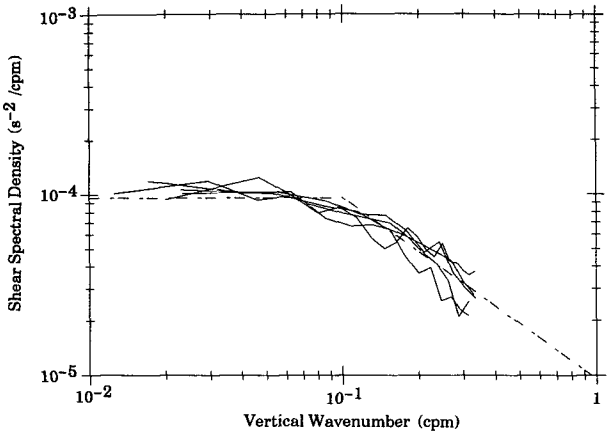

FIG. 2. Shear spectra scaled in the vertical by $1/E_1N^2$ and in the horizontal by E_1, and then divided by a factor of 2. The data are collapsed by this scaling. The five lines represent averages from 200–400, 400–1000, 1000–1500, 1500–2000, and 2000–3000 m for the reduced TOPO_Deep dataset. Two-piece band averaging has been employed.

4. Model–data comparison

Section 4a examines the buoyancy scaling of dissipation in a GM internal wave field. Wave fields exhibiting non-GM spectral characteristics are examined in section 4b. Non-GM spectral characteristics potentially invalidate the assumption of statistical stationarity in the GM-based dynamical models. Revisions to these models to accommodate non-GM spectral characteristics are discussed in section 2b.

a. The N dependence in a GM field

The finescale shears observed in the ocean interior, far from Fieberling Guyot (the TOPO_Deep dataset), are not differentiable from the GM prescription given the factor of 2 universality quoted for that model (Munk 1981). Shear/strain ratios are generally within a factor of 2 of the GM prescription ($R_\omega = 3$); the same holds true for the averaged shear spectral densities ($E_1 = 1$) (Table 2). Averaged shear spectra constructed with these data (Fig. 2) qualitatively fit the canonical scenario of uniform spectral density at large vertical scales out to a wavenumber m_c, defined by

$$m_c \int_0^{m_c} S_z dm = 0.7N_0^2$$

and falling as m^{-1} thereafter. The low wavenumber ($m < m_c$) spectral estimates are not significantly different (1 of 19 estimates exceeds the 95% confidence interval) from the revised GM76 spectrum assuming two degrees of freedom for each spectral estimate and that the two horizontal velocity components are statistically independent. The high wavenumber portion of the spectra is discussed elsewhere (Polzin 1992). Evidence for vertical anisotropy or horizontal polarization was ambiguous.

The shear/strain ratio is not, in general, independent of vertical wavenumber for these data. The tendency is for shear/strain ratio to increase toward lower wavenumber. The signal is not large however; the ratio varies less than a factor of 2. Nevertheless, such a trend implies that the wavenumber–frequency spectra are not separable. This issue is examined in greater detail in the section 4b, where the ratio for data from non-GM environments (containing more variability) is examined.

The TOPO_Deep dataset exhibits a variation of 140 in N^2, or a factor of 3.4 variation in $N^{1/2}$ [6.1 in $N^{1/2}\cosh^{-1}(N/f)$]. In contrast, the variation in E_1 and R_ω are minimal, factors of 1.7 and 1.6, respectively. A consequence of the latter is that the model expressions involving wave frequency were also nearly independent of depth; the MM term ($\alpha\langle\omega/f\rangle$) varied by a factor of 1.17, while the HWF term ($\alpha\langle k_h/m\rangle$) varied by 1.44. Thus, a test with these data of the various model N parameterizations is not masked by differences in the model's respective spectral level or frequency scalings.

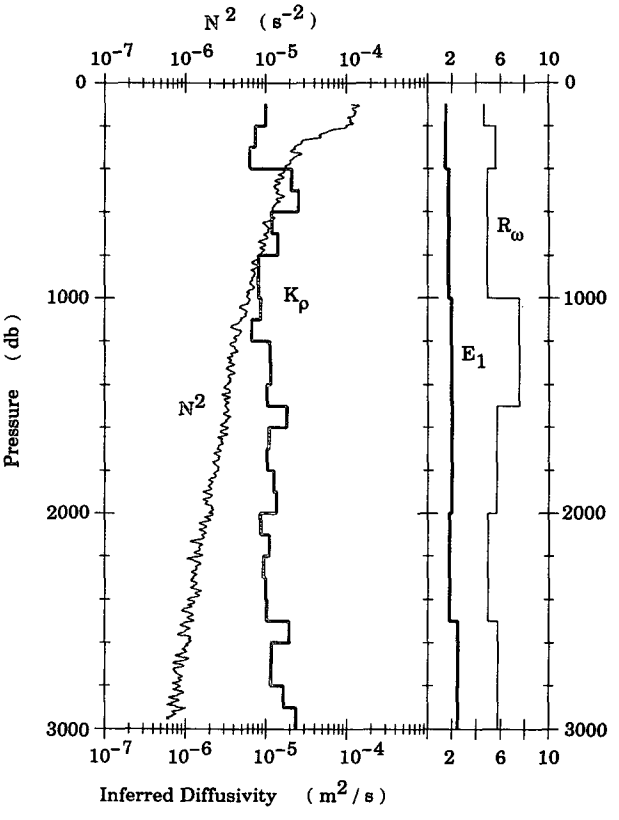

FIG. 3. Profiles of N^2, K_ρ, E_1, and R_ω. The N^2 values have been calculated with 20-db linear least-squares fits using the averaged temperature and salinity profiles. The inferred eddy diffusivities represent averages over 100 m. The E_1 and R_ω values have been averaged over the depth range of the bins delineated in Table 2.

The data were examined in seven depth bins as documented in Table 2 (which also contains the depth ranges over which the spectra were calculated). Profiles of N^2, E_1, R_ω, and K_ρ are presented in Fig. 3. In Fig. 3, as in Table 2, one finds that while N^2 varies by over two orders of magnitude, there is little variation in K_ρ. The result that $\epsilon \sim N^2$ as opposed to $\epsilon \sim N^{3/2}$ can be anticipated from this figure.

The four scalings under consideration are

$$(\mathrm{M})\ \epsilon = \hat{E}\frac{\sqrt{fN}}{\pi}\left(\frac{0.7(1+\ln(E_1))}{2\pi}\right)^{1/2} \times \exp\{-2/0.7(1+\ln(E_1))\} \quad [\text{Eq. (6)}]$$

$$(\mathrm{GH})\ \epsilon \sim EN^{3/2} \quad [\text{Eq. (5)}]$$

$$(\mathrm{MM})\ \epsilon \sim N^2E^2\alpha\langle\omega\rangle \quad [\text{Eq. (12)}]$$

$$(\mathrm{HWF})\ \epsilon \sim N^2E^2\alpha\frac{N}{f}\left\langle\left(\frac{\omega^2-f^2}{N^2-\omega^2}\right)^{1/2}\right\rangle \quad [\text{Eq. (11)}].$$

The following expressions are tested:

$$(\mathrm{M})\ K_\rho\left(\frac{N}{N_0}\right)^{1/2}\alpha_0/\alpha E_1(1+\ln(E_1))^{1/2} \times \exp\{-2/0.7(1+\ln(E_1))\}$$

$$(\mathrm{GH})\ K_\rho\left(\frac{N}{N_0}\right)^{1/2}\Big/E_1$$

$$(\mathrm{MM})\ K_\rho\alpha_0/\alpha\frac{\langle\omega\rangle}{f}E_1^2$$

$$(\mathrm{HWF})\ K_\rho\alpha_0/\alpha\frac{N}{f}\left\langle\left(\frac{\omega^2-f^2}{N^2-\omega^2}\right)^{1/2}\right\rangle\cosh^{-1}\left(\frac{N}{f}\right)E_1^2.$$

The scalings are presented versus buoyancy frequency in Fig. 4, such that the appropriate functional form should collapse the data onto a line parallel to the ordinate. Since for these data the largest difference in the model parameterizations is their N scaling, an inappropriate functional form in N will be revealed as a trend. Such a trend is associated with the Munk and GH ($\epsilon \sim N^{3/2}$) parameterizations. No such trend is apparent in the MM and HWF plots.

The error bars in Fig. 4 represent 95% confidence intervals. The confidence intervals for E_1 were calculated assuming chi-squared statistics for S_{z0} and two degrees of freedom for each Fourier coefficient. The confidence intervals for K_ρ were calculated via a bootstrap method (Efron and Gong 1983). Here, K_ρ values within each depth bin were vertically averaged over 10 m, yielding, according to run tests (Gregg et al. 1993b), statistically independent samples. The population of these 10-m values were repeatedly subsampled and averaged. The confidence intervals displayed represent the 3rd and 97th percentile of the distribution of 100 sums formed by randomly sampling one-half of the available data. These intervals are not substantially different from the 95% confidence intervals based upon a lognormal distribution (Baker and Gibson 1987). The total confidence intervals are calculated from the sum of the fractional errors in E_1 and K_ρ for the GH scaling and the sum of twice the fractional error in E_1 plus the fractional error in K_ρ for the other three scalings. No error estimate is offered for the estimates involving frequency content as we are uncertain about how to assess the error (see section 3). Geophysical data often do not meet the assumptions from which the statistical confidence intervals are calculated. However, given the obvious trends in the scaled data, we conclude that an $\epsilon \sim N^{3/2}$ scaling is inappropriate in a GM environment.

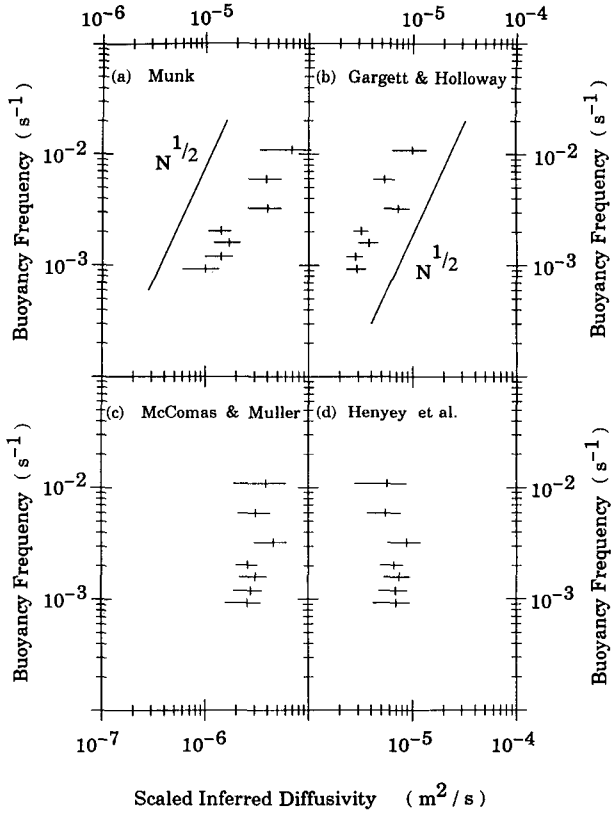

FIG. 4. Bin averages of the (a) Munk (1981), (b) Gargett and Holloway (1984), (c) McComas and Muller (1981), and (d) Henyey et al. scaling of the inferred diffusivity versus N, where K_ρ has units of $m^2\ s^{-1}$. The sloping line in (a) and (b) represents a $N^{1/2}$ dependence. The Munk and GH scaling reveal distinct trends with N and appear inconsistent with the data.

b. *Dissipation scaling in non-GM wave fields*

The data added here include the WRINCLE, TOPO_F, and NATRE profiles, along with the three deep segments from the TOPO_Deep profiles obtained over the seamount base. Documentation of the non-GM spectral characteristics precedes the model/data

comparison, which focuses on the extended HWF and MM models.

A vertical interval between 700 and 1300 m of the TOPO_F profiles was analyzed in three overlapped sections of 256 db (Table 3). The shear/strain ratios of this dataset were lower than any other (Table 3) and decrease toward the bottom, implying an increase of average wave frequency with depth. The ratio of alongslope to across-slope shear spectral density increased with depth, reaching a value of 1.5 for wavelengths larger than 40 m in the depth interval 1100–1300 db. Thus, this internal wave field is inhomogeneous. The enhancement of alongslope shear relative to across-slope shear is somewhat puzzling as it is opposite that expected from the internal wave reflection processes (e.g., Eriksen 1985). No signal denoting preferential vertical propagation was apparent in the rotary vertical spectra (e.g., Leaman and Sanford 1975).

Consistent with expectations for preferential generation (e.g., Rubenstein and Roberts 1986) and wave–mean flow interactions (e.g. Kunze 1985), the warm ring (WRINCLE) data exhibited large internal wave spectral levels and the highest shear/strain ratios we observed (Table 3). An average factor of 3 dominance of clockwise-with-depth polarized variance over counterclockwise at large scales ($m < m_c$) is taken as denoting a preponderance of downward energy propagation (Leaman and Sanford 1975). In a separate paper, Kunze et al. (1995) report excellent agreement between the estimated divergence of the vertical energy flux by these waves (presumably as they encounter critical layers below the vorticity bowl of the ring) and the kinetic energy dissipation. As noted above, our model comparisons ignore the relative vorticity. Use of Kunze's (1985) near-inertial dispersion relation and the corresponding expression involving shear/strain ratio yields model predictions for frequency content that differ by only 5%.

In comparison to the TOPO_Deep observations, the NATRE data exhibited higher spectral levels and greater shear–strain ratio with depth. These data were transformed in either 256- or 512-m pieces (Table 3). Analysis of these data indicated a pattern of enhanced northward shear relative to eastward shear at vertical wavelengths between 256 and 512 m with counterclockwise-with-depth variance exceeding clockwise by a factor of 50% on vertical wavelengths of (70–256 m). The observations thus represent marginally anisotropic, inhomogeneous conditions.

Unlike the TOPO_Deep data of section 4a (Fig. 2), shear spectra from the present sites did not follow the canonical pattern (Fig. 5). The TOPO_F and WRINCLE spectra are peaked about m_c. At low wavenumber, the NATRE spectral density conspicuously decreases with increasing wavenumber. In addition, the cutoff wavenumber of the NATRE spectra appears to occur at a higher shear variance, and the high wavenumber slope of the WRINCLE spectra appears to be appreciably steeper than -1. A possible dynamical explanation for this steeper slope is given in Polzin (1992). The low wavenumber behavior of the spectra is described much better by the modified canonical spectrum discussed in section 2b (Fig. 1c) than by a power law $(m/m_c)^p$ until m_c and thereafter as m^{-1} (Fig. 1b).

The shear/strain ratio is presented in Fig. 6. Here we have chosen to plot an integrated statistic,

$$\int_0^m S_z dm \Big/ N^2 \int_0^m F_z dm,$$

as a function of cumulative variance, $\int_0^m S_z dm$, for $\langle S^2 \rangle < 0.7N^2$. The statistic shows an increasing tendency at the lowest wavenumbers and decreasing at the highest. The variability in the NATRE and TOPO_Deep data exceeds that expected for a homogeneous population given 95% confidence intervals based upon the F distribution. The variability in the shear–strain statistic is regarded as implying that the frequency spectra are nonseparable. These observations of nonseparability cannot be immediately interpreted in the context of this study.

To begin the parameterization study, we first compare the dissipation predictions of the basic HWF model (4) with the observations (Fig. 7). The focus here is on the basic scaling of the model, not the magnitude of the predictions; correct scaling would be denoted by data points collapsing onto a line paralleling that drawn in Fig. 7. As shown, the HWF scaling appears to successfully account for much of the observed range in the inferred diffusivity; the data do roughly lie along a straight line. However, they fall well to the right of the agreement curve for the most part and, more troubling, exhibit a factor of 15 variation about a linear regression line (greatly exceeding the factor of 2–3 represented by the confidence intervals). Sensitivity of the model to specific wavefield parameters is examined below.

The dependence of dissipation upon the shear spectral level was examined for a restricted subset of the data: observations that satisfied $N^2 < 6.0 \times 10^{-6}$ s^{-2} and $4.6 < R_\omega < 8.2$. The restriction in stratification limited uncertainty in the buoyancy scaling of the models. For the restricted dataset, N^2 varied by a factor of 6.6. As before, the limitation in shear/strain ratio minimizes the influence of wave frequency in the comparison; the frequency corrections to the MM and HWF models for these data varied by factors of 1.2 and 1.5, respectively. The variability in E_1 (a factor of 4.9) thus greatly exceeded that of the other parameters. As demonstrated in Fig. 8, the variation of inferred diffusivity of the reduced data collapses under quadratic E_1 scaling: the factor of 1.5 scatter of the data points is less than the statistical uncertainty of each point. We therefore conclude that these data are consistent with a scaling of $\epsilon \sim E^2N^2$, the basic scaling exhibited by the McComas and Muller and Henyey et al. models.

We find no association between the observed dissipation and the low-wavenumber slope of the shear spectra in these data. For each of the available average shear

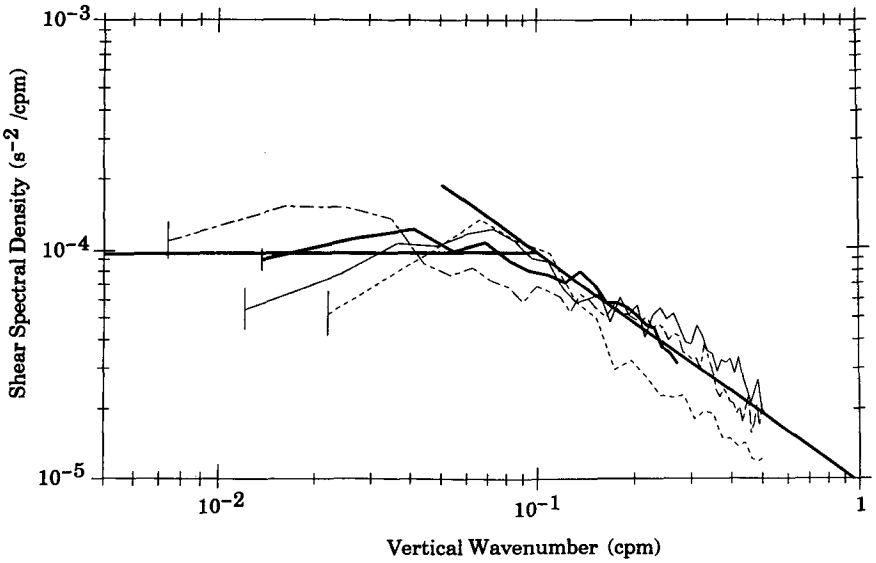

FIG. 5. Shear spectra scaled in the vertical by $1/E_1N^2$ and in the horizontal by E_1, and then divided by a factor of 2. The thick data line represents TOPO_DEEP data above 2000 db, the short-dashed curve WRINCLE data, the thin line TOPO_F data, and the long-dashed curve NATRE data from 500 to 2000 m. The solid straight line represents the GM76 spectrum out to 0.1 cpm, then falls as m^{-1}. The m^{-1} regime has been extended to lower wavenumber for comparison purposes. Two-piece band averaging has been employed for the NATRE spectra.

spectra, the low wavenumber slope p was estimated from linear least-squares fits to the spectral density estimates at wavenumbers smaller than m_c. The ensemble of inferred diffusivity estimates scaled by E_1^2 (the MM and HWF scaling) exhibits no dependence on p (Fig. 9). In particular, the HWF and MM model predictions of dissipation varying as $p + 1$ for $p < 0$ and independent of p for $p > 0$ is not supported by these data. Based on these results, we suggest that dissipation rates and, in turn, the net internal wave flux of energy through vertical wavenumber space, are not overly sensitive to spectral slope when the spectral levels are estimated in the manner employed here (13). This does not imply that the dynamics of internal wave–wave interactions is independent of the spectral slope. Theoretical reexamination of this issue is clearly called for: these data cannot distinguish which of the particular model assumptions used to derive the scaling result breaks down.

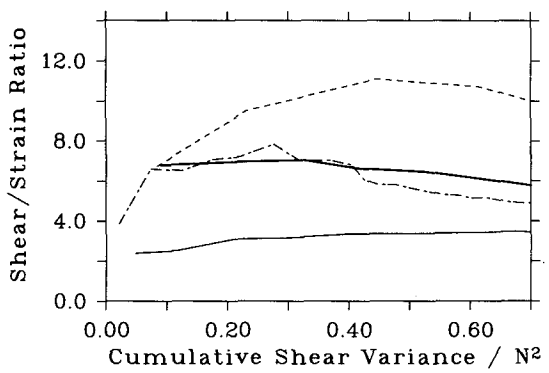

FIG. 6. The integrated shear/strain ratio vs cumulative shear variance. The thick solid line represents the TOPO_Deep data (100–2000 m); the dashed line indicates WRINCLE; the dot-dashed line denotes NATRE (500–2000 m); and the thin solid line is TOPO_F (700–1300 m).

In contrast, a consistent trend was observed between K_ρ/E_1^2 and R_ω (Fig. 10). Theoretically this association is expected as R_ω is related to the MM and HWF frequency corrections (11) and (12). For a given finescale shear spectral level, greater dissipations are observed in wave fields characterized by higher average wave frequency (smaller R_ω). The full HWF and MM parameterizations for these data including our estimates of the frequency corrections are presented in Figs. 11 and 12. The following expressions are tested:

$$\text{(MM)}\quad [0.25\epsilon_{\mathrm{MM}}(E_{\mathrm{GM}}, N_0)/N_0^2]\frac{f}{f_0}E_1^2\frac{\alpha}{\alpha_0}\frac{\langle\omega\rangle}{f}\Big/ \frac{\langle\omega\rangle}{f}\mathrm{GM}, \frac{\langle\omega\rangle}{f}\mathrm{GM} = 1.41$$

$$\text{(HWF)}\quad [0.25\epsilon_{\mathrm{HWF}}(E_{\mathrm{GM}}, N_0)/N_0^2]\frac{f}{f_0}E_1^2\frac{\alpha}{\alpha_0}\frac{N}{f} \times \left\langle\left(\frac{\omega^2 - f^2}{N^2 - \omega^2}\right)^{1/2}\right\rangle \cosh^{-1}\left(\frac{N}{f}\right)\Big/\cosh^{-1}\left(\frac{N_0}{f_0}\right),$$

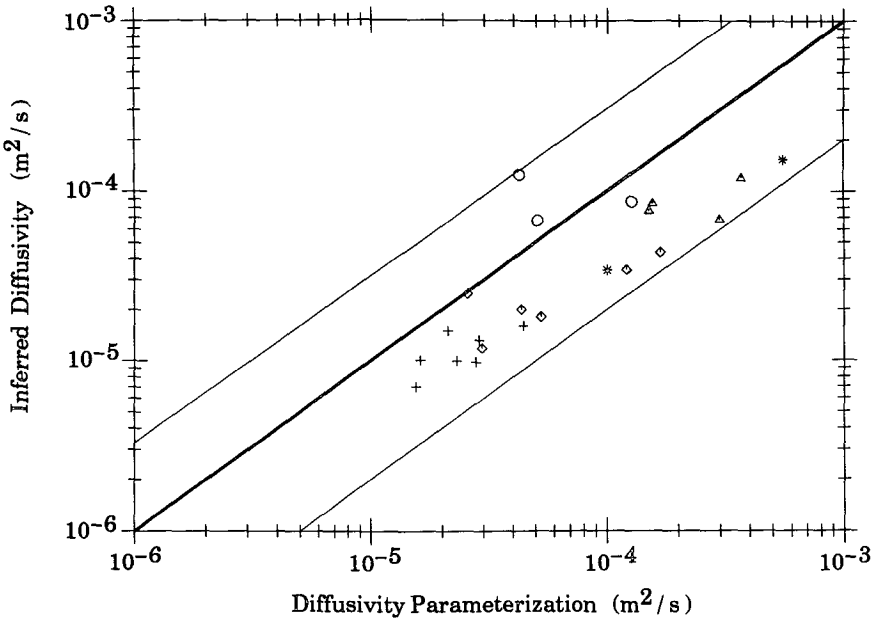

FIG. 7. Inferred diffusivities plotted as a function of $0.25\epsilon_{HWF}E_1^2/N^2$, where ϵ_{HWF} is the HWF dissipation estimate for GM spectral levels (4). The thick line denotes agreement with the model and the thin lines bound the outliers. Plus signs denote the TOPO_Deep data, asterisks the TOPO_Deep data exhibiting heightened spectral levels below 2000 m, circles the TOPO_F data, triangles the WRINCLE data, and diamonds the NATRE data.

where the GM specification of

$$\frac{N}{f}\left\langle\left(\frac{\omega^2-f^2}{N^2-\omega^2}\right)^{1/2}\right\rangle$$

is 1.0, f_0 is appropriate for 32.5°N, and ϵ_{MM} and ϵ_{HWF} are from (1) and (4), respectively.

The frequency corrections effectively collapse the data: the variability of the predictions about the observations exhibited after employing the MM scaling is a factor of 4; that remaining in the HWF scaling is less than a factor of 2. Both high (TOPO_F) and low (WRINCLE) frequency data appear as outliers in the MM scaling. The low-frequency data do not appear as outliers in the HWF parameterization. More significantly, the models are differentiable in terms of their predictions for the magnitude of the dissipation. In the present study, the HWF model estimates and data are not distinguishable, whereas the MM model overpredicts the data by a factor of 4, on average.

These results suggest that variability in the E_1-scaled inferred diffusivities from non-GM environments is primarily associated with the frequency distribution of the internal wave field. The accuracy of the shear/strain ratio as a proxy for average wave frequency is examined in appendix B. There it is concluded that for a broadband wave field, the shear/strain ratio method returns values biased toward the GM value. That is, the expected wave frequency tends to be underestimated for high-frequency wave fields and overestimated for wave fields dominated by low-frequency motions. This tendency is most significant for wave fields characterized by high frequency waves where the difference between the expected value and that deduced from the shear/strain ratio approaches a factor of 2. Consistent with this idea, the TOPO_F dissipations from a high frequency wave field are underpredicted by the dynamical models (presumably because the average wave frequency is underestimated). We conclude that more accurate estimation of the expected value of wave field frequency than afforded by the shear/strain ratio would substantially reduce the remaining scatter in the model dissipation predictions.

In summary, the observed buoyancy scaling for internal wave fields that exhibit GM spectral shapes was shown to be consistent with $\epsilon \sim N^2$. A subset of the data with limited variability in N and frequency content was consistent with a quadratic spectral level scaling, $\epsilon \sim E^2$. Significant deviations from an $\epsilon \sim E^2N^2$ scaling are observed for internal wave fields that exhibit characteristics indicative of non-GM frequency content, that is, non-GM frequency spectral shapes. A simple revision to the HWF model, which accounts for non-GM wave frequency content, successfully explained most of this variability. Deviations from GM vertical wavenumber shapes were found not to be closely related to variability of the observed dissipation rates. Given the success of the revised HWF model in collapsing the observed dissipation rates within the limitations of the shear/strain-based estimate of fre-

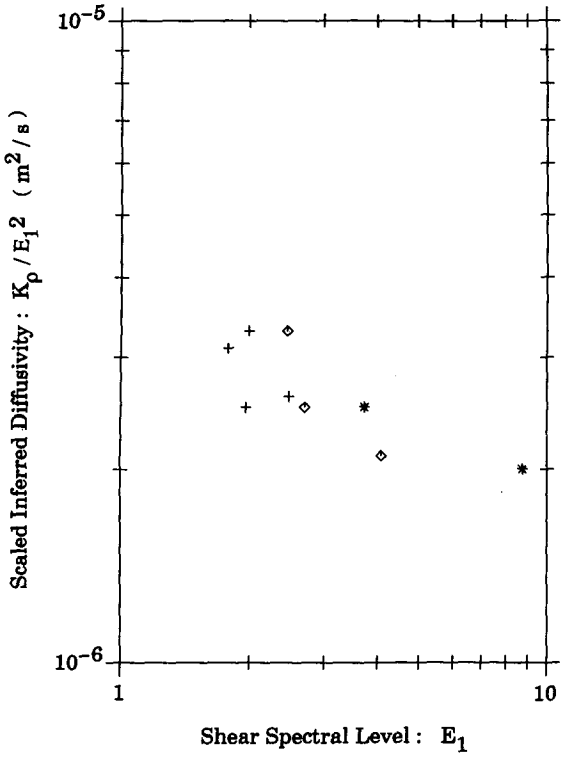

FIG. 8. Estimates of K_ρ/E_1^2 vs spectral level, E_1. Plus signs denote the TOPO_Deep data, asterisks the TOPO_Deep data exhibiting heightened spectral levels below 2000 m, and diamonds the NATRE data.

quency content, we infer that anisotropy and inhomogeneity are similarly ineffective in affecting the dissipation rate.

5. Conclusions and discussion

The predicted scalings of four models relating internal wave processes to the rate of dissipation of turbulent kinetic energy ϵ were examined. First, data exhibiting internal wave characteristics consistent with the GM76 model (given the factor of 2 universality quoted for that model) were analyzed. For these data, the scalings of Gargett and Holloway (1986), also Gargett (1990), and that of Munk (1981) (i.e., $\epsilon \sim N^{3/2}$) were determined to be inconsistent with an observed buoyancy scaling of approximately N^2. Combination of these data with an examination of a restricted database with near-constant N and average wave frequency revealed a scaling consistent with $\epsilon \sim N^2E^2$, the scaling of two dynamical models (Henyey et al. 1986; McComas and Muller 1981b).

Both dynamical models are predicated on the GM internal wave prescription (and modest departures from it). As well, these theories include predictions for how dissipation is affected by non-GM spectral characteristics of varying frequency/vertical wavenumber spectral shapes. Consistent with the theories, we find association between dissipation and the average frequency of the internal wave field. The Henyey et al. scaling, $\epsilon \sim (\omega^2 - f^2)^{1/2}$, was found to collapse the data more effectively than the scaling of McComas and Muller ($\epsilon \sim \omega$). Moreover, the dissipation estimates agree in magnitude with the model of Henyey et al., while the model of McComas and Muller overpredicts the dissipation rate by a factor of 4. We find no association between dissipation and the shape of the vertical wavenumber spectrum at low wavenumber. The present datasets encompassed spectra with low wavenumber slopes with vertical wavenumber ranging between −0.6 and +0.9. This is a discrepancy with the models and calls for further theoretical study.

If the remaining variability between data and model can be attributed to error in the shear/strain ratio–based frequency estimate, then anisotropy, inhomogeneity, and nonseparability would appear to be nonissues. We have reported theoretical arguments that suggest the directionality of the wave field is not im-

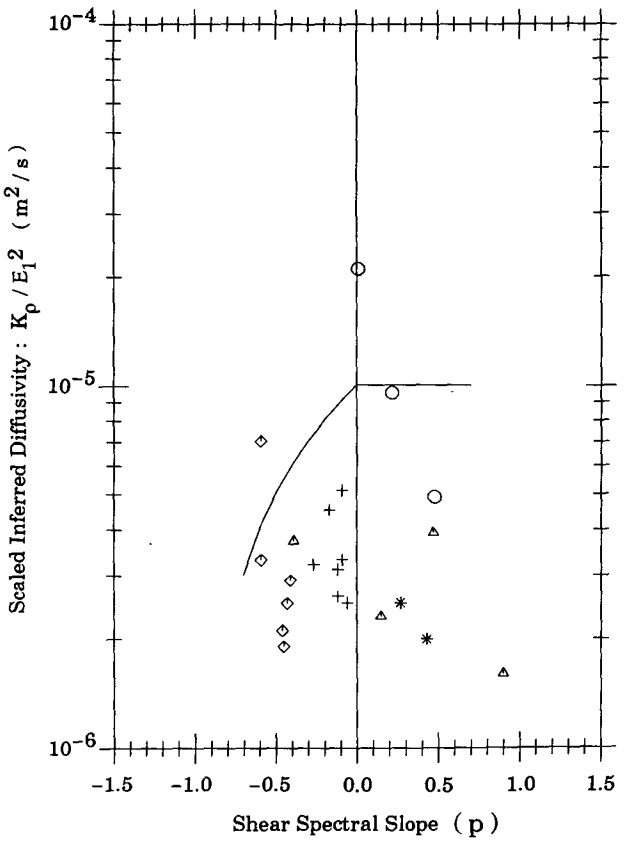

FIG. 9. Estimates of K_ρ/E_1^2 versus the shear spectral slope (p) for wavenumbers smaller than m_c. The solid line denotes the trend predicted by extensions to the HWF and MM models. Plus signs denote the TOPO_Deep data, asterisks the TOPO_Deep data exhibiting heightened spectral levels below 2000 m, circles the TOPO_F data, triangles the WRINCLE data, and diamonds the NATRE data.

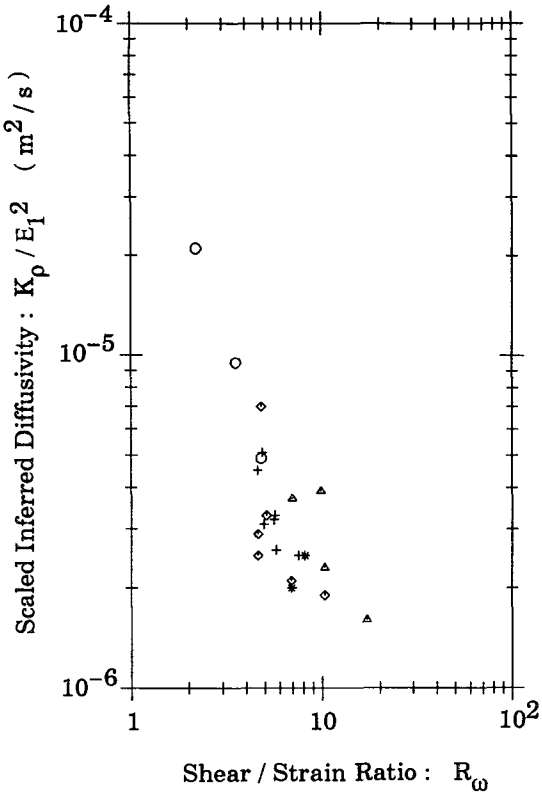

FIG. 10. Bin averages of K_ρ/E_1^2 plotted vs the shear–strain ratio R_ω. Plus signs denote the TOPO_Deep data, asterisks the TOPO_Deep data exhibiting heightened spectral levels below 2000 m, circles the TOPO_F data, triangles the WRINCLE data, and diamonds the NATRE data. A consistent trend between the two variables is apparent and implies that variability in the E-scaled estimates of inferred diffusivity is associated with the frequency content of the internal wave field.

portant in determining the net up-wavenumber energy flux at small scales. However, this issue has not been formally addressed in the context of either dynamical model. The GM spectrum is separable, and furthermore, the GM based models suggest that the GM vertical wavenumber spectrum is stationary so that the dissipation rate may be equated with the up-wavenumber energy flux of the models at arbitrary wavenumber. However, these same models predict energy fluxes through frequency space, which imply an equilibrium vertical wavenumber/frequency spectrum that is nonseparable. We have pursued corrections to the models under the assumption that deviations from the GM spectrum could be addressed separately in wavenumber and frequency. If the equilibrium spectrum is not separable, this is not entirely true and the corrections that have been applied might not be appropriate for data that exhibit nonseparable characteristics. However, we are of the opinion that corrections for nonseparable characteristics are of higher order than those pursued. All three issues need further investigation.

Kunze et al. (1995) find remarkable agreement between the observed dissipation rate in the WRINCLE dataset and calculations based upon wave–mean flow interaction dynamics. This is surprising since we have demonstrated that much of these same data are consistent with an internal wave–wave interaction scaling. Since both Kunze et al. (1995) and the HWF model are based upon ray tracing results, the relative wave–wave and wave–mean flow interaction strengths can be compared by examining scale estimates for the rate of change of vertical wavenumber. From Kunze et al. (1995), $dm/dt = -\frac{1}{2}\zeta_z \sim 0.5\ (.15f)/300\ \text{m} = 3 \times 10^{-8}\ \text{m}^{-1}\ \text{s}^{-1}$. From the HWF model the average velocity is approximately $dm/dt \approx \mathbf{U}_z \cdot \mathbf{k}_h = |U_z k_h| \times (1 - r)/(1 + r)$. At m_c, $dm/dt \sim \sqrt{0.7}\, N(0.4) N^{-1} f m_c(0.26) \sim 9 \times 10^{-7}\ \text{m}^{-1}\ \text{s}^{-1}$. At $m_c/2$, however, the two estimates are comparable. While wave–wave interaction rates are in general larger than wave–mean flow interactions at all scales resolved in this study, it is not until a sufficiently small scale is reached that the *average* wave–wave fluxes dominate. With wave–mean flow rates dominating the average wave–wave interaction rates at large scales and the opposite at small scales, it may not be entirely coincidental that the estimates of energy flux divergence, energy flux through the vertical wavenumber spectrum, and observed dissipation rates agree.

Gargett (1990) criticized the study of Gregg (1989) as suffering from a biased estimate of E at high spectral levels (see the introduction). One implication of this criticism was that Gregg's warm core ring (RING 82I) and PATCHEX data would not be collapsed under the GM E^2N^2 scaling if an unbiased estimator for E was employed. We suspect that Gregg's RING 82I data was dominated by near-inertial motions. The present study has demonstrated that at a given spectral level, a low frequency wave field will correspond to lower than expected dissipations (11). It is our conjecture that Gregg was able to collapse his PATCHEX and RING 82I datasets under the E^2N^2 scaling due to a cancellation between the underestimation of E and the lower than expected dissipations associated with lower than average wave frequency. In another dataset, DRIFTER, Gregg's E^2N^2-based dissipation estimate overpredicted the observed dissipation in a region dominated by a near-inertial feature. The shear variance associated with that feature was sufficiently small that his estimate of the spectral level was relatively unbiased, and his findings therefore conform to our expectations.

We are aware of only one other dataset that documents the necessary frequency/vertical wavenumber information to test the ideas set forth in this paper. Wijesekera et al. (1993) tested GM-based versions of MM and HWF outlined in section 2a with data from non-GM environments. They concluded that a simple E^2N^2 parameterization was inappropriate for those data and in turn examined variations in total internal wave energy ($\hat{E}$) in combination with variations in the

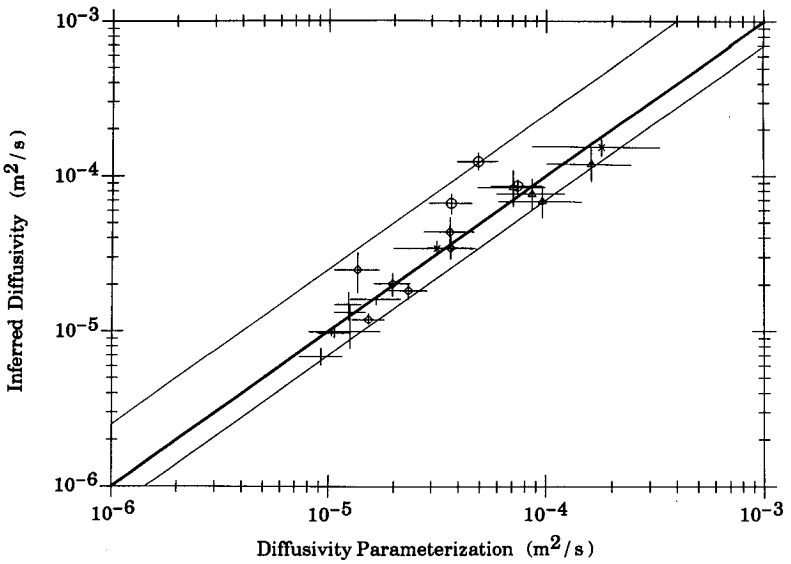

FIG. 11. Bin-averaged inferred diffusivities K_ρ plotted versus the revised Henyey et al. parameterization. The thick line denotes the model prediction; the thin lines bracket the outliers. The WRINCLE data are represented by triangles, the TOPO_F data by circles, the TOPO_DEEP data by plus signs and asterisks, and the NATRE data by diamonds. The crosses denote 95% confidence intervals.

low-mode bandwidth of the energy spectrum (i.e., j_*). Their procedure essentially constituted an examination of the variability associated with changes in the shape of the vertical wavenumber spectrum. They found significant discrepancies between the GM-based models and their observed dissipation rates, consistent with the findings above that the slope of the vertical wavenumber spectrum is not associated with variability in

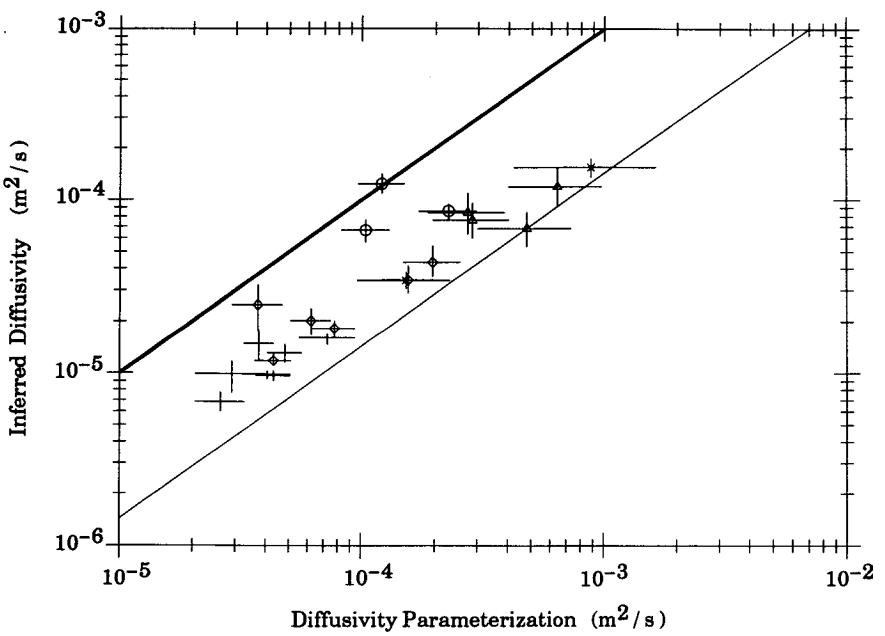

FIG. 12. Bin-averaged diffusivities K_ρ plotted vs the revised McComas and Muller parameterization. The thick line denotes the model prediction; the thin lines bracket the outliers. The WRINCLE data are represented by triangles, the TOPO_F data by circles, the TOPO_Deep data by plus signs and asterisks, and the NATRE data diamonds. The crosses denote 95% confidence intervals.

the observed dissipations. The internal wave field in that dataset contained significant contributions from the semidiurnal tide and higher frequencies. Padman and Dillon (1991) reported that the most energetic mixing events were associated with the presence of high frequency internal wave packets.

Wijesekera et al. (1993) also examined the GH and Gregg (1989) scalings and a strain-based estimator. They concluded the best parameterization was an ad hoc scheme in which the GM normalized strain variance was substituted for the shear variance in Gregg's (1989) scaling. We suggest that the viability of the strain-based parameterization over Gregg (1989) was linked to lower shear/strain ratio for these high frequency internal waves. As a simple test of this assertion, the shear–strain ratio–based corrections to the HWF model in section 2b were applied to the Gregg (1989) parameterization (17) for the data given in Wijesekera et al.:

$$\epsilon_{17} = \epsilon_{G89} \frac{\alpha}{\alpha_0} \frac{N}{f} \left(\frac{\omega^2 - f^2}{N^2 - \omega^2} \right)^{1/2} \tag{17}$$

with

$$\epsilon_{G89} = 7 \times 10^{-10} \frac{\langle N^2 \rangle}{N_0^2} \frac{\langle S^2 \rangle^2}{S_{GM^2}^2} \text{ W kg}^{-1},$$

$$\epsilon_{\lambda} = 7 \times 10^{-10} \frac{\langle N^2 \rangle}{N_0^2} \frac{\langle \lambda^2 \rangle^2}{\lambda_{GM^2}^2} \text{ W kg}^{-1},$$

and

$$R_\omega = 3 \left(\frac{\epsilon_{G89}}{\epsilon_{\lambda}} \right)^{1/2}.$$

The relevant numbers were obtained by inverting results from Wijesekera et al.'s Table 4 and appear in our Table 4. The capabilities of the simple frequency-based correction to Gregg (1989) and the strain-based estimator appear to be equally impressive in collapsing the dissipation data of Wijesekera et al. (1993). The results of this exercise are published with the following caveats. The first difference operator employed by Wijesekera et al. potentially represents a biased estimator (Gargett 1990). Second, the shear and strain spectra do not exhibit the same cutoffs in vertical wavenumber. This is presumed to be a universal result and is the subject of a forthcoming manuscript. Third, these data exhibit nonseparable characteristics.

The present results, which support the Henyey et al. dissipation parameterization, have immediate implications for oceanic mixing driven by internal wave motions. First, mixing, as denoted by an inferred eddy diffusivity (at constant flux Richardson number), is constant in the main thermocline for a wave field that exhibits GM spectral levels and frequency characteristics. Moreover, the background vertical mixing rates for the GM76 spectral representation are small:

TABLE 4. Abstracted results from Wijesekera et al. (1993) with dissipation predictions based on the extended HWF model and terms derived from data in Wijesekera et al.'s Table 4. The time periods and depth ranges represent the binning structure chosen by Wijesekera et al. The Gregg (1989) (ϵ_{G89}) scaling significantly underestimates ϵ, whereas Wijesekera et al.'s strain-based scaling (ϵ_λ) and a simple frequency correction to Gregg (1989) (ϵ_{17}) work reasonably well.

Period	Nominal depth range (m)	$\frac{\epsilon_{G89}}{\langle\epsilon\rangle}$	$\frac{\epsilon_\lambda}{\langle\epsilon\rangle}$	$\frac{\epsilon_{17}}{\langle\epsilon\rangle}$
2	100–170	0.14	0.21	0.17
	170–220	0.30	0.73	0.50
	220–270	0.25	2.10	1.65
3	100–170	0.12	0.90	0.70
	170–220	0.10	1.13	1.90
	220–270	0.10	2.11	2.82
4	100–170	0.06	0.77	2.07
	170–220	0.50	1.03	0.75
	220–270	0.50	1.05	0.75

$K_\rho(E_{GM})$ is approximately 7×10^{-6} m^2 s^{-1} (with $R_f = 0.2$). These results validate the assertions of Gregg (1989). Some variation in the observed value of K_ρ in the thermocline may be expected due to heightened spectral levels associated with the interaction of internal waves with the mesoscale vorticity field (e.g., Kunze 1985) or with seasonal fluctuations in surface forcing (e.g., Briscoe and Weller 1984). Quantification of variability in the thermocline awaits better models of internal wave generation by surface forcing mechanisms. Second, since the data are inconsistent with an inverse scaling of K_ρ with N at constant E, some process or collection of processes must be responsible for heightened E values in the abyss if internal waves alone are responsible for producing the O[1 − 10(× 10^{-4} m^2 s^{-1})] diffusivities generally inferred from hydrographic data and box models. We view bottom reflection (e.g., Eriksen 1985) and/or bottom generation (e.g., Bell 1975) processes to be likely candidates: values of K_ρ in excess of 1×10^{-4} m s^{-1} are evident in most of our profiles, which are near topographic features. We find the results sufficiently encouraging to warrant further investigation into the efficacy of bottom affected internal waves in producing globally averaged abyssal diffusivities of O(10^{-4} m^2 s^{-1}).

Acknowledgments. We wish to thank Eric Kunze for helpful discussions and suggestions and the detailed advice of two anonymous reviewers. Support was provided under Grants N00014-89-J-1073 and N00014-92-J-1323 from the Office of Naval Research and from the National Science Foundation.

APPENDIX A

Internal Wave Models

The purpose of this appendix is to describe in detail the steps taken in the formulation of the model–data

comparison. Notation not appearing in Table 1 is consistent with the respective papers in which it appears.

a. McComas and Muller (1981b)

These investigators equate dissipation with the sum of the id and psi energy fluxes past an arbitrary vertical wavenumber ($\beta_* < \beta < \beta_c$) under the assumption of statistical stationarity. The energy flux under the induced diffusion mechanism was determined by the boundary conditions with the low-frequency portion of the spectrum and accounted for approximately 40% of the total energy flux (Muller et al. 1986). Hence, $\epsilon = Q_{\text{psi}}/0.6$. Note that Gregg (1989) assumed an equality between the two mechanisms on the basis of a 1988 personal communication from P. Muller.

Under the assumption of stationarity, MM estimated the psi fluxes at $\beta_* = 2\pi m_*$ as the loss of energy from waves at $(\beta, \omega) = \beta_*, 2f)$ to waves at $(x\beta_*, f)$ $(x = \sqrt{10})$ and at $(x\beta_c, f)$ as the gain of energy from waves at $(\beta_c, 2f)$. With the assumption of a frequency energy density of the form ω^{-2}, MM's estimate of the flux at large scales can be written as

$$Q_{\text{psi}} = \frac{27}{x32}\frac{\pi f}{N^2}\beta_*^2 E^2,$$

where E is the total energy of the internal wave field (not to be confused with the E in Table 4). In this form, the flux estimate requires estimation of both β_* and E. These variables are difficult to estimate accurately [e.g., Wijesekera et al. (1993)]. The MM model can be equivalently expressed at small scales. For a frequency energy spectrum of the form ω^{-2}, MM's equation (4.11) can be simply rewritten as

$$Q_{\text{psi}} = \frac{27}{x32}\frac{\pi f}{N^2}\{\alpha\hat{S}(x\beta_c)\hat{S}(\beta_c)\},$$

where α retains its definition in Table 4, and $\hat{S}$ is a vertical wavenumber shear density spectrum with units of $\text{s}^{-2}\ \text{m}^{-1}$ [$\hat{S} = \beta^{-1}S(\beta)$, so that $S(\beta)$ is the shear content spectrum of MM]. Identification of β_c with the break in the spectral slope m_c renders the use of E_1 as an estimate of the spectral level to be consistent with the MM model.

b. Henyey, Wright, and Flatté (1986)

Henyey et al. employed the Munk (1981) version of the GM spectrum. This version differs from GM76 in two respects. The first involves the low vertical wavenumber form of the energy density: $(m + m_*)^{-2}$ (GM76) versus $(m^2 + m_*^2)^{-1}$ (Munk 1981). The spectral levels in Munk (1981) were adjusted so that the integral (i.e., the energy) equalled that of GM76. This adjustment affects the model shear variance estimate. For wavenumbers smaller than 0.1 cpm, $\langle S^2\rangle = 0.7N^2$ (GM76) and $0.5N^2$ (Munk 1981). This difference was apparently unintentional. For a detailed discussion, see Gregg and Kunze (1991). Munk's second modification to the GM spectrum consisted of the addition of an extra m^{-1} dependence for vertical wavenumbers greater than 0.1 cpm. For this work we have assumed GM76 spectral levels and a cutoff vertical wavenumber defined by

$$\langle S^2\rangle = \int_0^{m_c} S_z dm = 0.7N^2.$$

To uniformly evaluate the various model expressions under the GM76 model employed here, the HWF expression for the dissipation rate needs to be adjusted. Under the assumption that the ratio between up- and down-wavenumber fluxes r is a function only of the shear variance in waves of larger scale (HWF, Henyey 1991), (3) can be solved for $r(m)$ given $S_z(m)$ under the assumption that the vertical wavenumber spectrum is stationary. In particular, at $\langle S^2\rangle = 0.5N^2$, $r = 0.76$ for Munk (1981). For GM76 at $\langle S^2\rangle = 0.5N^2$, $m = \frac{5}{7} \times 0.1$ cpm. This leads to an expression for the dissipation rate that is greater than the published result of HWF by a factor of $(7/5)^2$.

APPENDIX B

Frequency Content Estimates

In this work the shear/strain ratio is used to diagnose the frequency content in non-GM wave fields. The factor involving frequency in the dynamical models is most properly given by its expected value. The shear/strain procedure employed here may not provide accurate estimates of the expected values for the following reasons. First, employing the shear/strain ratio to estimate frequency is equivalent to asserting that the variance of a broadband wave field resides in a single wave. The extent to which this is not true in a GM field is revealed in the disparity between the expected value (10) and the shear/strain-based estimates of k_h/m and ω, (15) and (16) quoted in section 3. The consistency of the estimates is examined in detail below. Second, high-frequency internal waves ($\omega > 10f$) have been tentatively identified as having greater shear than is predicted by linear theory (Anderson 1992).

The shear/strain-based expressions might be said to be at least consistent estimators of the expected value if they revealed the same range of variability as the expected value for frequency spectra of arbitrary shape. A general description for the frequency spectrum (neglecting tidal components) of the form $\omega^{-q}(\omega^2 - f^2)^{-p}$ can be had in terms of the strength of an inertial peak $(\omega^2 - f^2)^{-p}$, $p < 1$ and a high-frequency slope, $-(q + 2p)$. In Fig. A1, the ratio of the expected value of Nk_h/f_m (10) to that derived from the shear/strain ratio (16) is contoured as functions of p and $(q + 2p)$. [The ratio has been further normalized so that the estimators agree at GM conditions ($p = \frac{1}{2}$, $q = 1$) with $N = N_0$ and $f = 1 \times 10^{-4}\ \text{s}^{-1}$.] Clearly, the functional depen-

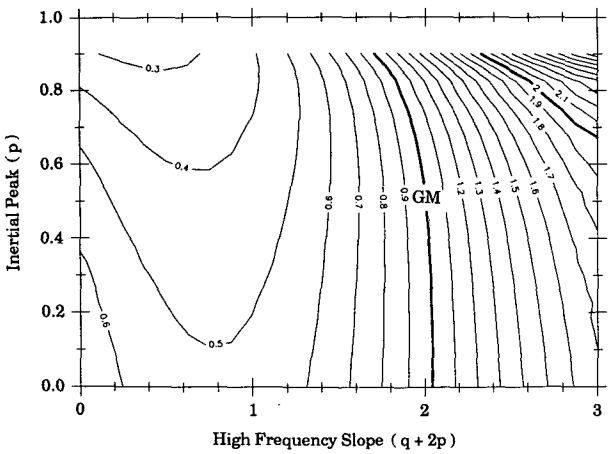

FIG. A1. Contoured estimates of the ratio between $(N/f)[(\omega^2 - f^2)/(N^2 - \omega^2)]^{1/2}$ derived from (14) and the expected value weighted by the frequency spectrum (10). The ratio is contoured as a function of the strength of the inertial peak (p) and the high-frequency slope ($p + 2q$) for a frequency spectrum of the form $\omega^{-q}(\omega^2 - f^2)^{-p}$. The GM specification $[(p, q) = (1/2, 1)]$ is denoted by the symbol "GM."

dences of the two estimators (10) and (16) upon p and q are not the same, and thus the estimates are not, in general, consistent.

There is in Fig. A1, however, a distinct pattern. The shear/strain predictor tends to underestimate the expected value in a wave field characterized by excess high-frequency energy (flatter than GM high frequency spectrum, smaller inertial peak) and, conversely, to overestimate the expected value in a low frequency wave field (stronger inertial peak, steeper spectral roll off at high frequency). The implication is that the present correction factors employed in the dissipation predictors are biased toward the GM value. Dissipation predictions in a high frequency wave field may be underestimated; those in a low frequency field may be overestimated. This tendency is observed in our observations.

REFERENCES

Anderson, S. P., 1992: Shear, strain and thermohaline fine structure in the upper ocean. Ph.D. dissertation, University of California, San Diego, 173 pp.

Baker, M. A., and C. H. Gibson, 1987: Sampling turbulence in the stratified ocean: Statistical consequences of strong intermittency. *J. Phys. Oceanogr.*, **17**, 1817–1836.

Bell, T. H., 1975: Topographically generated internal waves in the open ocean. *J. Geophys. Res.*, **80**, 320–327.

Bray, N. A., and N. P. Fofonoff, 1981: Available potential energy for MODE eddies. *J. Phys. Oceanogr.*, **11**, 30–46.

Briscoe, M. G., and R. A. Weller, 1984: Preliminary results from the Long-Term Upper-Ocean Study (LOTUS). *Dyn. Atmos. Oceans*, **8**, 243–265.

Cairns, J. L., and G. O. Williams, 1976: Internal wave observations from a midwater float. 2. *J. Geophys. Res.*, **81**, 1943–1950.

Duda, T. F., and C. S. Cox, 1989: Vertical wavenumber spectra of velocity and shear at small internal wave scales. *J. Geophys. Res.*, **94**, 939–950.

Efron, B., and G. Gong, 1983: A leisurely look at the bootstrap, the jackknife, and cross-validation. *Amer. Stat.*, **37**, 36–48.

Eriksen, C. C., 1982: Observations of internal wave reflection off sloping bottoms. *J. Geophys. Res.*, **87**, 525–538.

——, 1985: Implications of ocean bottom reflection for internal wave spectra and mixing. *J. Phys. Oceanogr.*, **15**, 1145–1156.

Flatté, S. M., F. S. Henyey, and J. A. Wright, 1985: Eikonal calculations of short-wavelength internal wave spectra. *J. Geophys. Res.*, **90**, 7265–7272.

Fofonoff, N. P., 1969: Spectral characteristics of internal waves in the ocean. *Deep-Sea Res.*, **16**(Suppl.), 59–71.

Gargett, A. E., 1990: Do we really know how to scale the turbulent kinetic energy dissipation rate ϵ due to braking of oceanic internal waves? *J. Geophys. Res.*, **95**, 15 971–15 974.

——, and G. Holloway, 1984: Dissipation and diffusion by internal wave breaking. *J. Mar. Res.*, **42**, 15–27.

——, P. J. Hendricks, T. B. Sanford, T. R. Osborn, and A. J. Williams III, 1981: A composite spectrum of vertical shear in the ocean. *J. Phys. Oceanogr.*, **11**, 1258–1271.

Garrett, C. J. R., and W. H. Munk, 1975: Space–time scales of internal waves: A progress report. *J. Geophys. Res.*, **80**, 291–297.

Gregg, M. C., 1989: Scaling turbulent dissipation in the thermocline. *J. Geophys. Res.*, **94**, 9686–9698.

——, and T. B. Sanford, 1988: The dependence of turbulent dissipation on stratification in a diffusively stable thermocline. *J. Geophys. Res.*, **93**, 12 381–12 392.

——, and E. Kunze, 1991: Internal wave shear and strain in Santa Monica Basin. *J. Geophys. Res.*, **96**, 16 709–16 719.

——, D. P. Winkel, and T. B. Sanford, 1993a: Varieties of fully resolved spectra of vertical shear. *J. Phys. Oceanogr.*, **23**, 124–141.

——, H. E. Sein, and D. B. Percival, 1993b: Statistics of shear and turbulent dissipation profiles in random internal wave fields. *J. Phys. Oceanogr.*, **23**, 1777–1799.

Hayes, S. P., H. B. Milburn, and E. F. Ford, 1984: TOPS: A free-fall velocity and CTD profiler. *J. Atmos. Oceanic Technol.*, **1**, 220–236.

Henyey, F. S., 1991: Scaling of internal wave model predictions for ϵ, dynamics of oceanic internal gravity waves. *Proc. 'Aha Huliko'a Hawaiian Winter Workshop*, P. Muller and D. Henderson, Eds., University Hawaii at Manoa, Honolulu, pp. 233–236.

——, and N. Pomphrey, 1983: Eikonal description of internal wave interactions: A non-diffusive picture of Induced Diffusion. *Dyn. Atmos. Oceans*, **7**, 189–219.

——, J. Wright, and S. M. Flatté, 1986: Energy and action flow through the internal wave field: An eikonal approach. *J. Geophys. Res.*, **91**, 8487–8495.

Itsweire, E. C., J. R. Koseff, D. A. Briggs, and J. H. Ferziger, 1993: Turbulence in stratified shear flows: Implications for interpreting shear induced mixing in the ocean. *J. Phys. Oceanogr.*, **23**, 1508–1522.

Kunze, E., 1985: Near-inertial wave propagation in geostrophic shear. *J. Phys. Oceanogr.*, **15**, 544–565.

——, 1986: The mean and near-inertial velocity fields in a warm-core ring. *J. Phys. Oceanogr.*, **16**, 1444–1461.

——, 1993: Submesoscale dynamics near a seamount. Part II: The partition of energy between internal waves and geostrophy. *J. Phys. Oceanogr.*, **23**, 2589–2601.

——, and T. B. Sanford, 1993: Submesoscale dynamics near a seamount. Part I: Measurements of Ertel vorticity. *J. Phys. Oceanogr.*, **23**, 2567–2588.

——, A. J. Williams III, and M. G. Briscoe, 1990: Observations of shear and vertical stability from a neutrally buoyant float. *J. Geophys. Res.*, **95**, 18 127–18 142.

——, M. A. Kennelly, and T. B. Sanford, 1992: The depth-dependence of shear finestructure off Point Arena and near Pioneer Seamount. *J. Phys. Oceanogr.*, **22**, 29–41.

——, R. W. Schmitt, and J. M. Toole, 1995: The energy balance in a warm core ring's near-inertial critical layer. *J. Phys. Oceanogr.*, **25**, in press.

Leaman, K. D., and T. B. Sanford, 1975: Vertical energy propagation of inertial waves: A vector spectral analysis of velocity profiles. *J. Geophys. Res.*, **80,** 1975–1978.

McComas, C. H., and P. Muller, 1981a: Time scales of resonant interactions among oceanic internal waves. *J. Phys. Oceanogr.*, **11,** 139–147.

——, and P. Muller, 1981b: The dynamic balance of internal waves. *J. Phys. Oceanogr.*, **11,** 970–986.

Muller, P., G. Holloway, F. Henyey, and N. Pomphrey, 1986: Nonlinear interactions among internal gravity waves. *Rev. Geophys.*, **24,** 493–536.

Munk, W., 1981: Internal waves and small-scale processes. *Evolution of Physical Oceanography,* B. A. Warren and C. Wunsch, Eds., The MIT Press, 264–291.

Nasmyth, P., 1970: Oceanic turbulence. Ph.D. dissertation, Institute of Oceanography, University of British Columbia, 69 pp.

Oakey, N. S., 1982: Determination of the rate of dissipation of turbulent energy from simultaneous temperature and velocity microstructure measurements. *J. Phys. Oceanogr.*, **12,** 256–271.

Osborn, T. R., 1974: Vertical profiling of velocity microstructure. *J. Phys. Oceanogr.*, **4,** 109–115.

——, 1980: Estimates of the local rate of vertical diffusion from dissipation measurements. *J. Phys. Oceanogr.*, **10,** 83–89.

Padman, L., and T. M. Dillon, 1991: Turbulent mixing near the Yermak Plateau during CEAREX. *J. Geophys. Res.*, **96,** 4769–4782.

Polzin, K. L., 1992: Observations of turbulence, internal waves and background flows: An inquiry into the relationships between scales of motion. Ph.D. dissertation, MIT/WHOI Joint Program in Oceanography, Tech. Rep. No. WHOI-92-39, 244 pp.

——, and E. T. Montgomery, 1995: Microstructure processing for the High-Resolution Profiler (HRP). WHOI Tech. Rep., in press.

Rossby, T., 1988: Five drifters in a Mediterranean salt lens. *Deep-Sea Res.*, **35,** 1653–1663.

Rubenstein, D. M., and G. O. Roberts, 1986: Scattering of inertial waves by an ocean front. *J. Phys. Oceanogr.*, **16,** 121–131.

Schmitt, R. W., J. M. Toole, R. L. Koehler, E. C. Mellinger, and K. W. Doherty, 1988: The development of a fine- and microstructure profiler. *J. Atmos. Oceanic Technol.*, **5,** 484–500.

Siedler, G., and U. Paul, 1991: Barotropic and baroclinic tidal currents in the eastern basins of the North Atlantic. *J. Geophys. Res.*, **96,** 22 259–22 271.

Wijesekera, H., L. Padman, T. Dillon, M. Levine, C. Paulson, and R. Pinkel, 1993: The application of internal-wave dissipation models to a region of strong mixing. *J. Phys. Oceanogr.*, **23,** 269–286.

Wunsch, C., and S. Webb, 1979: The climatology of deep ocean internal waves. *J. Phys. Oceanogr.*, **9,** 235–243.

Yamazaki, H., and T. R. Osborn, 1990: Dissipation estimates for stratified turbulence. *J. Geophys. Res.*, **95,** 9739–9744.